Predicting large experimental excess pressure drops for Boger fluids in contraction-expansion flow

H.R. Tamaddon-Jahromi , I.E. Garduño , J.E. López-Aguilar , M.F. Webster

PII: S0377-0257(16)00032-X
DOI: 10.1016/j.jnnfm.2016.01.019
Reference: JNNFM 3750

To appear in: *Journal of Non-Newtonian Fluid Mechanics*

Received date: 19 October 2015
Revised date: 27 January 2016
Accepted date: 30 January 2016

Please cite this article as: H.R. Tamaddon-Jahromi , I.E. Garduño , J.E. López-Aguilar , M.F. Webster , Predicting large experimental excess pressure drops for Boger fluids in contraction-expansion flow, *Journal of Non-Newtonian Fluid Mechanics* (2016), doi: 10.1016/j.jnnfm.2016.01.019

Highlights

- A swanINNFM model reflects *epd* in axisymmetric contraction-expansion flows
- No counterpart *epd* is observed in planar configurations
- Over 200% Boger fluid enhanced pressure drops captured above Newtonian
- Rothstein & McKinley [1] experimental pressure-drop data is quantitatively captured
- Transition states detected between flow phases of steady, oscillatory and unstable form
- Flow-rate increase exhibits larger *epd* compared to fluid-relaxation time increase

Predicting large experimental excess pressure drops for Boger fluids in contraction-expansion flow

H.R.Tamaddon-Jahromi, I.E. Garduño, J. E. López-Aguilar, and M.F. Webster[†]

Institute of Non-Newtonian Fluid Mechanics, Swansea University, College of Engineering, Bay Campus, Fabian Way, Swansea, SA1 8EN, UK

Abstract

More recent finite element/volume studies on pressure-drops in contraction flows have introduced a variety of constitutive models to compare and contrast the competing influences of extensional viscosity, normal stress and shear-thinning. In this study, the ability of an extensional White–Metzner construction with FENE-CR model is explored to reflect enhanced excess pressure drops (*epd*) in axisymmetric 4:1:4 contraction-expansion flows. Solvent-fraction is taken as β=0.9, to mimic viscoelastic constant shear-viscosity Boger fluids. The experimental pressure-drop data of Rothstein & McKinley [1] has been *quantitatively* captured (in the initial pronounced rise with elasticity, and limiting plateau-patterns), via two modes of numerical prediction: (i) flow-rate *Q*-increase, and (ii) relaxation-time λ_1-increase. Here, the former *Q*-increase mode, in line with experimental procedures, has proved the more effective, generating significantly larger enhanced-*epd*. This is accompanied with dramatically enhanced trends with *De*-incrementation in vortex-activity, and significantly larger extrema in N_1, shear-stress and related extensional and shear velocity-gradient components. In contrast, the λ_1-increase counterpart trends remain somewhat invariant to elasticity rise. Moreover, under *Q*-increase and with elasticity rise, a pattern of *flow transition* has been identified through three flow-phases in *epd*-data; (i) steady solutions for low-to-moderate elasticity levels, (ii) oscillatory solutions in the moderate elasticity regime (coinciding with Rothstein & McKinley [1] data), and (iii) finally solution divergence. New to this hybrid algorithmic formulation are - techniques in time discretisation, discrete treatment of pressure terms, compatible stress/velocity-gradient representation; handling ABS-correction in the constitutive equation, which provides consistent material-property prediction; and introducing purely-extensional velocity-gradient component specification at the shear-free centre flow-line through the velocity gradient (VGR) correction.

Keywords: Viscoelastic fluid; pressure-drop prediction; extensional White–Metzner_FENE-CR model; axisymmetric contraction-expansion

[†] Correspondence Author: *E-mail address*: m.f.webster@swan.ac.uk

Introduction

This article considers predictive methods for the accurate capture of experimental levels of excess pressure drop *(epd*) in contraction-expansion flow situations, now a classical and elusive challenge to computational rheology. The geometric-ratio adopted is that of 4:1:4, and the study explores various alternative constitutive models to analyse and address this problem. This work follows a second partner-study on the dual problem of flow-past-a-sphere and the capture of enhanced drag (Garduño et al. [2]. Of the many constitutive models proposed, here particular advantage has been taken of the FENE-type construction, see Chilcott and Rallison [3]; alongside other models with more dissipative contributions, of viscoelastic White-Metzner (WM)-form. This approach has gainfully lead to the development and application of a hybrid class of models, introducing a dissipative function whilst combining the merits of both White-Metzner and FENE-CR models. In the dissipative function, $\varphi(\lambda_D\dot{\varepsilon})$, itself dependent on a material dissipative extensional-viscous time-scale (λ_D) and an extension-rate ($\dot{\varepsilon}$), here two approximations have proved of substantial benefit in large *epd*-capture – the full $\cosh(\lambda_D\dot{\varepsilon})$-form, and its truncated equivalent form $1+(\lambda_D\dot{\varepsilon})^2$.

The experimental background is such that, Nigen and Walters [4] found significant differences in pressure-drop between Boger and Newtonian liquids for axisymmetric flow. However, *no distinction* could be drawn between corresponding pressure drops for Newtonian and Boger fluids in *planar configurations*. Likewise, Rothstein and McKinley [5, 1] switched attention to axisymmetric contraction-expansion geometries of various contraction ratios (between two and eight) and degrees of re-entrant corner curvature, covering a large range of Deborah numbers. There large *epd* was observed for Boger fluids, above that for a Newtonian fluid, independent of contraction-ratio and re-entrant corner curvature. Furthermore, Rodd *et al.* [6] considered microfabricated contraction-expansion geometries (16:1:16, planar, sharp), investigating vortex generation, pressure-drops and the complex relationships between inertial and elastic influences. For a large range of Weissenberg numbers, the length-scale of the geometry was found important to generate strong viscoelastic effects, which were non-reproducible for the same fluid when using macro-scale geometries. In this manner, significant upstream vortex growth was generated alongside increase in excess pressure-drop of some 200 percent.

Computational prediction has somewhat lagged behind the above advances made experimentally. In the infancy of computational rheology, the so-called Upper-Convected Maxwell model (UCM) and the Oldroyd-B model (with solvent addition) were strongly favoured. This was partly due to their mathematical simplicity, whilst mimicking sufficiently complex rheometrical behaviour for the class of polymer solutions known as Boger fluids, made popular in the late 1970s (Boger [7]). In their early predictive work for L-shaped geometry flows, Perera and Walters [8] described the effects of increasing elasticity in viscoelastic flows. There a *decrease* in pressure-drop was reported as *elasticity increased* for a four-constant, shear thinning Oldroyd model (now known to be due to the shear-thinning contribution). In contrast, it was shown that by *increasing inertia* through Reynolds number, the pressure-drop was found to increase almost five orders higher than that observed upon increasing elasticity. The work of Debbaut *et al.* [9] and of Binding [10] already provided strong

hints as to the likely causes of the inadequacy of the Oldroyd B model in its under-prediction of the observed experimental increases in excess pressure drop (*epd*). Nevertheless, the outstanding question and computational challenge on contraction-flow pressure-drops remains: when and under what conditions could a constant shear-viscosity/strain-hardening viscoelastic fluid reflect experimental enhanced *epd,* as experienced under axisymmetric flow settings for Boger fluids.

It is now well accepted that the increase in Couette correction for Boger fluids flowing in axisymmetric contractions can be very high indeed. The various contributions clearly present the theoretical and computational rheologist with some significant challenges, some of which on vortex dynamics for example, have already been resolved (*see* Phillips and Williams [11]; Aboubacar *et al.* [12]; Walters and Webster [13]; Alves *et al.* [14]). Moreover, the POLYFLOW finite element package with Oldroyd models and an EVSS formulation (Binding *et al.*, [15]), has provided some *epd*-results for 4:1:4 planar and axisymmetric contraction-expansion geometries with solvent-fraction viscosity-ratios of β=0.9 and 1/9 (see on for definition). With increasing Deborah number (*De*) and the larger β=0.9 ratio, an increase in *epd* was reported in the planar context, with upturn and modest enhancement (of O(1~2%); whilst under the axisymmetric context, only upturn without enhancement was observed. In addition and more recently, Pérez-Camacho *et al.* [16] have examined a Newtonian, Boger, and shear-thinning polymer solutions for various contraction-ratios (2:1:2, 4:1:4, 6:1:6, 8:1:8, 10:1:10). There, particular attention has been given to the pressure-drops and kinematics obtained experimentally, in a flow apparatus specifically designed for the purpose. These authors found computationally that pressure-drops revealed a relationship between N_1 and extensional viscosity for both Boger and shear-thinning solutions, and that enhanced-*epd* could be extracted experimentally for ratio-factors of 4 and above.

This present paper stands as a continuation of our previous work on this problem (Aguayo *et al.* [17]; Walters *et al.* [18], Tamaddon-Jahromi *et al.*, [19, 20], in predicting pressure-drop for Boger-type fluids in contraction-expansion flows. There, a variety of new models have been explored, all with a single relaxation mode, constant shear-viscosity and extensional-viscosity, in common with Oldroyd-B. A general conclusion of these earlier numerical findings (Walters *et al.* [18, 21]), have confirmed earlier comments by Binding [10] and Debbaut and Crochet [3] that, whereas *high extensional viscosity* levels can give rise to *large increases* in the *epd*, *increasing normal-stress difference* levels can have the *opposite effect*. In addition to generate enhanced-*epd*, the levels of stress must be raised across the constriction, for which the fluid rheology plays a key role (Aguayo *et al.* [17]). Moreover, Walters *et al.* [21], attempted to show how some generalizations of the original White-Metzner model could help to understand the competing influence of various rheometrical functions on important flow characteristics. Adopting this line of approach, Tamaddon-Jahromi *et al.* [19], proposed a constitutive model with the combined extensional viscosity functionality of Debbaut and Crochet [3], and the shear-thinning viscoelastic Linear Phan-Thien-Tanner (LPTT) model. There, experimental–levels of *epd*-enhancement were successfully derived with flow-rate increase, and also somewhat in line with the experimental range of deformation-rates reported. However, there were limitations to this finding, in that modest shear-thinning was introduced, and that the viscoelastic component itself was limited in range and effectiveness on enhancement (as purely viscous dissipative models, also gave similar, with slightly less *epd*-enhancement).

2. Problem specification - governing equations and constitutive models

Incompressible and isothermal viscoelastic flow is governed by mass and momentum conservation principles, along with an equation of state for the material. In dimensionless form, balance equations under these conditions may be expressed as:

$$\nabla \cdot \mathbf{u} = 0 \tag{1}$$

$$\mathrm{Re}\frac{\partial \mathbf{u}}{\partial t} = -\mathrm{Re}\,\mathbf{u}\cdot\nabla\mathbf{u} + \nabla\cdot\boldsymbol{T} - \nabla p, \tag{2}$$

where $\boldsymbol{T} = \boldsymbol{\tau} + 2\beta\mathbf{d}$, is the total stress. This is decomposed into a Newtonian solvent contribution $(2\beta\mathbf{d})$, and a viscoelastic polymeric contribution $\boldsymbol{\tau}$. In eqs.(1)-(2), **u**, $\mathbf{d} = \frac{1}{2}(\nabla\mathbf{u} + \nabla\mathbf{u}^{\dagger})$, and p represent fluid velocity, rate-of-deformation, and hydrodynamic pressure, respectively. Throughout the flow is assumed to be creeping flow (Re ≈ $O(10^{-2})$), and as a consequence, the momentum convection term has negligible contribution. Here, superscript notation † denotes tensor transpose. The solvent fraction parameter β is defined as $\beta = \frac{\eta_{\text{solvent}}}{\eta_{\text{solvent}} + \eta_{\text{polymeric}}}$, where η_{solvent} and $\eta_{\text{polymeric}}$ are the Newtonian solvent and zero-rate polymeric viscosity contributions.

In this paper, the relevant equations of state are introduced, alongside a comprehensive listing in Tables1-2 for all constitutive variants discussed and their rheometrical functions. Firstly, the constitutive equation for the FENE-CR model (Chilcott and Rallison [22]) provides the following expression for the conformation tensor:

$$De\,\overset{\nabla}{\mathbf{A}} + \mathrm{f}\left[\mathrm{Tr}(\mathbf{A})\right](\mathbf{A} - \mathrm{I}) = 0. \tag{3}$$

Here, $\mathrm{f}\left[\mathrm{Tr}(\mathbf{A})\right]$ is the stretch-function. This stretch-function is affected by the extensibility parameter L, which modulates the influence of $\mathrm{Tr}(\mathbf{A})$ as:

$$\mathrm{f}(\mathrm{Tr}(\mathbf{A})) = \frac{1}{1 - \mathrm{Tr}(\mathbf{A})/\mathrm{L}^2}. \tag{4}$$

In eqs. (3)-(4), Reynolds and Deborah group numbers may be defined as: $\mathrm{Re} = \rho\dot{\gamma}_{\text{avg}}\bar{\mathrm{L}}^2/(\eta_{\text{solvent}} + \eta_{\text{polymeric}})$, $De = \lambda_1\dot{\gamma}_{\text{avg}}$, where ρ represents material density, and $\dot{\gamma}_{avg} = \frac{\bar{U}}{\bar{L}}$ is the average shear-rate in the constriction zone, with average velocity $\bar{U}$ across the constricted region, and characteristic length $\bar{L}$ equal to constriction radius $R_c = R_U/4$ (see Figure 1). For the 4:1:4 contraction-expansion flow, Rothstein and McKinley [5, 1] introduced the Deborah number as: $De_{\lambda_1}^{\text{EXP}} = \lambda_1\frac{\mathrm{Q}}{\pi\mathrm{R}_c^3}$, with flow rate ($0<Q\leq 0.5$ cm^3/sec), constriction radius (R_c=0.3175cm), and relaxation time of

λ_1=0.146sec (see Appendix I for scaling factor equivalence on Deborah numbers from experiments to simulation). One notes in passing that, *De*-incrementation may be gathered under (i) elevation of flow-rate, *Q*-increase (rise in average velocity $\bar{U}$, mode preferred experimentally), or under (ii) elevation of fluid elastic-memory (λ_1-increase, mode favoured computationally). Below, this issue is explored in some depth.

Kramers' rule in eq.(5) is the means to translate the conformation tensor into its counterpart stress tensor form:

$$\boldsymbol{\tau} = \frac{(1-\beta)}{De} f\left[Tr(\mathbf{A})\right]\mathbf{A}. \tag{5}$$

ABS-f-correction Furthermore and in the context of complex 4:1:4 contraction-expansion flow of wormlike micellar fluids, López-Aguilar *et al.* [30] provided evidence of negative dissipation function values being generated during flow evolution and along the spatial domain. In turn, this provoked negative values of the f_τ−functional (leading to negative viscosity predictions) when approaching numerical *Wi*-solution breakdown. Hence to eliminate this source of inconsistency, the absolute-value operation was applied to each term of the dissipation function in the associated f_τ−functional. Correspondingly, to avoid such a possibility arising under FENE-CR-type models, an ABS-correction has been applied similarly to the f−functional of eq. (4), where the absolute-value operation is taken to apply to each constituent component of the trace function (Tr(|**A**|). This correction has strong influence on numerical tractability at relatively larger *De*-levels, whilst remaining invariant within the underlying theoretical predictions in simple shear and uniaxial extensional flows. The corresponding ***ABS-f -correction*** is then:

$$\mathrm{f}(\mathrm{Tr}(\mathbf{A})) = \frac{1}{1-\mathrm{Tr}(|\mathbf{A}|)/\mathrm{L}^2_{\mathrm{FENE}}}. \tag{6}$$

This analysis also investigates a viscoelastic extensional polymer-network-based White-Metnzer model (White and Metzner [23]). The White-Metzner (WM) theoretical framework assumes that a flowing polymeric-material consists of a long chain of molecules connected in a continuously changing network, for which junctions vanish in a limited time. In this work, a modification to the base White-Metzner expressions is considered. Here, the viscosity η is modified to be a function of second ($\boldsymbol{II}_d$) and third ($\boldsymbol{III}_d$) invariants of the rate-of-deformation tensor, where expressions for generalised shear-rate and extension-rate in complex flow may be taken as,

$$\boldsymbol{II}_d = \frac{1}{2}\mathrm{tr}\left(\mathbf{d}^2\right), \quad \boldsymbol{III}_d = det\left(\mathbf{d}\right). \tag{7}$$

By design, such a modified White-Metzner model introduces extensional hardening effects.

In a similar hybrid fashion, the FENE-CR model may also be modified with an extension-rate-dependent viscosity, rendering an *extensional White-Metzner FENE-CR* model (eWM_FENE-CR). Adapting eq.5 and accounting for both viscous and polymeric contributions, this hybrid combination of a White–Metzner construction with a FENE-CR model, eWM(*Cosh*)/FENE, may be expressed in the form:

$$\boldsymbol{T} = \frac{(1-\beta)}{De}\,\mathrm{f}\left[\mathrm{Tr}(\mathbf{A})\right]\mathbf{A}\phi(\dot{\varepsilon}) + 2\beta\phi(\dot{\varepsilon})\mathbf{d}, \tag{8}$$

where $\dot{\varepsilon}$ is the extensional strain rate defined as $\dot{\varepsilon} = 3\mathbf{III}_d / \mathbf{II}_d$. The dissipative function $\phi(\dot{\varepsilon})$ is defined in eq. (9) below. In particular, note here that the FENE-CR contribution remains in terms of the conformation-tensor. The hyperbolic viscosity law of Debbaut and Crochet [3] and Debbaut *et al.* [9] is adopted for this version of eWM_FENE-CR, as:

$$\phi(\dot{\varepsilon}) = \cosh\left(\lambda_D\dot{\varepsilon}\right) \tag{9a}$$

or, its preferred quadratic-term truncated Taylor series approximation,

$$\phi(\dot{\varepsilon}) \approx 1 + \left(\lambda_D\dot{\varepsilon}\right)^2 \tag{9b}$$

see alternative truncated forms of $\phi(\dot{\varepsilon})$ in Appendix-II. Note, the form for the rheometrical functions for these models, as provided in Table 2, where in particular, the magnifying product influence of the dissipative function $\phi(\dot{\varepsilon})$ is apparent on the extensional viscosity. Henceforth, to render model naming more succinct, the choice is made to replace the form eWM_FENE-CR, with more simply swanINNFM, using (c) or (q) appendage to indicate type of hyperbolic or quadratic dissipative function.

The next phase of study is targeted at adjustment of the extensional viscosity response alone, essentially layered upon the rheology of the foregoing models with no additional influence upon N_1 and η_s. This departs somewhat from the Oldroyd-B form for η_e (unbounded, sharp change around $De = 2\lambda_1\dot{\varepsilon}$), while anticipating a wider exploration of deformation-rate space (Figure 2). The goal now becomes that of identifying the balance between η_e and N_1 as deformation-rate rises, and capturing significant *epd* in line with experimental findings.

Here, two new viscoelastic hybrid White-Metzner/FENE-CR model forms are deployed; namely the $\cosh\left(\lambda_D\dot{\varepsilon}\right)$ function form (eq. 9a), now swanINNFM(c), and a second, with a quadratic approximation of the cosh function $1+\left(\lambda_D\dot{\varepsilon}\right)^2$ (eq. 9b), now swanINNFM(q). The elongational-dependence of these two functions may be introduced into the separate solvent and polymeric contributions, individually (purely dissipative) or in combination (dissipative/recoverable). The extensional viscosity of these two new models is shown in Figure 2 for the range of $0.1 \le \lambda_D \le 4.0$. Here, an increasing trend in η_e is clearly apparent for both swanINNFM forms when compared to the FENE-CR model. Sharp increase in extensional viscosities is displayed for larger value of λ_D=4.0 around the strain-rate of O(0.1) units. For lowers value of λ_D=0.1 and λ_D=0.5, the extensional viscosities (η_e) of both WM models follow the η_e

of FENE-CR up to strain-rates of around O(3) and O(2) units, respectively. Again, a sharp increase in η_e is observed for both models as the strain-rate increases.

3. Numerical schemes and discrete problem approximations

3.1 Hybrid finite element/finite volume scheme The hybrid finite element/volume scheme utilised is a semi-implicit, time-splitting, fractional-staged formulation. This invokes finite element (*fe*) discretisation for velocity-pressure, alongside cell-vertex finite volume (*fv*) sub-cell approximation for stress (see Webster *et al.* [24], Matallah *et al.* [25]). Over triangles in two dimensions, this leads to a parent-cell quadratic-linear velocity-pressure *fe*-approximation, with a four-subtended triangular child-cell *fv*-approximation within each parent-cell. Overall, the algorithm is based on a two-step Lax-Wendroff splitting (Donea [26], Zienkiewicz [27]), crafted around an incremental pressure-correction procedure to satisfy incompressibility (conservation of mass). With a forward time-increment, such a three-stage pressure-correction implementation provides second-order temporal accuracy.

Conservation of mass, momentum & finite-element scheme Galerkin discretisation may be applied to the Stokesian sections of the system; the momentum equation at Stage 1, the pressure-correction at Stage 2 and the incompressibility correction constraint at Stage 3. For reasons of accuracy, an element-by-element Jacobi scheme is used to solve the resulting Galerkin Mass matrix-vector equations at Stages 1 (momentum) and Stage 3, requiring only a handful of iterations. With only a single matrix reduction phase necessary at the initial stage, Stage 2a is handled through a direct Choleski decomposition procedure. Finally, pressure and diffusive terms at Stages 1a and 1b are treated in semi-implicit form, to enhance stability. Pressure temporal treatment calls upon multi-step reference across three successive time-levels.

Constitutive eq. & finite-volume scheme Cell-vertex *fv*-schemes applied to the conformation-tensor equation are based upon an upwinding technique (fluctuation distribution) on each triangular *fv*-child-cell. This distributes control volume residuals to provide nodal solution updates (Wapperom and Webster [28]). The non-conservative form of the conformation-tensor equation [eq. (3)] may be treated by gathering flux-terms into a flux-contribution $\boldsymbol{R} = \mathbf{u} \cdot \nabla \mathbf{A}$, and grouping the remaining terms under the source-contribution ($\boldsymbol{Q}$).The objective is to evaluate the flux and source variations over each finite volume triangle (Ω_l), with their distribution to its three vertices according to the preferred strategy. The resulting nodal update for a particular node (l) is obtained by accumulating the contributions from its control volume Ω_l, composed of all *fv*-triangles surrounding node (l). The flux and source residuals may be evaluated over different control volumes associated with a given node (l) within the *fv*-cell T; namely, the flux contribution governed over the *fv*-triangle T, (R_T, Q_T), and that subtended over the median-dual-cell zone, (R_{mdc}, Q_{mdc}). This procedure demands appropriate area-weighting to maintain consistency, which for temporal accuracy has been extended to time-terms likewise (see further details in the references cited above Aboubacar *et al.* [29]).

Problem specification & mesh refinement The benchmark problem studied is that of creeping flow (Re ≈ O(10^{-2})) within a 4:1:4 axisymmetric contraction-expansion with rounded contraction-cap and corners (Figure 1, schematic and meshes). Here, solvent fractions of 90% are taken as standard (β=0.9), to represent the low-solvent balance

and constant shear-viscosity of typical Boger fluids (Boger [7]). Three successively refined meshes (see Figure 1 detail) have been utilised in this study (following Aguayo *et al.* [17]), to ensure present solution consistency with mesh refinement to within 0.1% accuracy across primary solution variables. As such, all solutions are reported on the medium refinement mesh.

VGR-correction* & *imposition of* c*entreline shear-free boundary conditions This velocity gradient modification has been introduced specifically to prevent noise proliferation in the pursuit of high-*De* solutions [30]. The VGR-correction is imposed at the centreline, where shear-free extensional flow prevails. This pure extensional-deformation condition is enforced by imposing: (i) null values onto the shear velocity-gradient components (shear-free flow), thus ensuring 1D-extensional deformation (eq. 10); (ii) pure uniaxial-extension relationship between the normal velocity-gradient components (eq. 11); and (iii) nodal-pointwise continuity imposed exactly, in discrete form (eq. 12). Note that, in the constitutive equation, condition (iii) has been imposed throughout the domain to meet conservation of mass. Conditions (i)-(iii) under VGR-correction become:

$$\frac{\partial u_z}{\partial r} = \frac{\partial u_r}{\partial z} = 0, \tag{10}$$

$$\frac{\partial u_r}{\partial r} = -\frac{1}{2}\frac{\partial u_z}{\partial z} = -\frac{1}{2}\hat{\dot{\varepsilon}}, \tag{11}$$

$$\frac{u_r}{r} = -\left(\frac{\partial u_z}{\partial z} + \frac{\partial u_r}{\partial r}\right) = -\frac{1}{2}\hat{\dot{\varepsilon}}. \tag{12}$$

In the above, $\hat{\dot{\varepsilon}} = \frac{\partial u_z}{\partial z}$ represents the strain-rate on the centreline in the axial direction, a region of pure uniaxial (non-homogeneous) extensional deformation.

4. Earlier work, some background and prior results

In an earlier study with the FENE equations-of-state, Szabo *et al.* [31] provided solutions for such a 4:1:4 contraction-expansion flow, and concluded that the total dissipation rate resulted from the product of the pressure-drop times the flow-rate. Moreover, the 4:1:4 contraction-expansion problem was found to be more computationally tractable than its counterpart for 4:1 contraction flows. This is due to the balanced inlet-outlet configuration (periodic in kinematics/stress), which generates significantly smaller pressure-drops in the contraction-expansion setting, proving an order of magnitude lower than those for contraction flows (Walters *et al.* [18, 21]). In this work, the flow-domain meshing is composed of 1080 quadratic elements and 2289 nodes with 14339 degrees of freedom. Such a problem setting has been vigorously studied by Aguayo *et al.* [17], which provides for a thorough mesh refinement analysis and much further detail, see Figure 1b.

The *excess pressure-drop* (*epd*), itself is defined as the ratio between the pressure-drop for a Boger fluid (subscript B in eq.(12)) to that for a corresponding Newtonian fluid (subscript N) (Szabo *et al.* [31], Aguayo *et al.* [17], and Binding *et al.* [15]). This amounts to a relative Couette correction between the two fluids:

$$epd = \frac{\left(\Delta p - \Delta p_{fd}\right)_{\mathrm{B}}}{\left(\Delta p - \Delta p_{fd}\right)_{\mathrm{N}}}, \quad \Delta p_{fd} = \Delta p_u L_u + \Delta p_d L_d . \tag{13}$$

In this notation, Δp is the total pressure-drop between the inlet and outlet zones, where fully-developed flow is ensured; Δp_u is the fully-developed pressure-gradient generated in the *upstream* section, Δp_d is the fully-developed pressure-gradient in the *downstream* section; and L_u and L_d are upstream and downstream lengths, respectively. Note in the present study, experimental 4:1:4 axisymmetric contraction-expansion *epd*-data for polystyrene Boger-fluids (Rothstein and McKinley [5, 1]) may be compared directly against the numerical predictions for *epd*, for the various constitutive models proposed.

4.1 Effect of normal stress (N_1) and extensional viscosity (η_e) on epd : Models A-D, α, J, and FENE-CR models – some earlier simulation predictions

In this section, a summary of our earlier numerical results (Walters *et al.* [18, 21], Tamaddon-Jahromi *et al.* [20, 32]) are presented in Figures 3-5 and Tables 1-3. There, these models introduced and explained share the same constant shear viscosity as for Oldroyd-B, whilst others share common Oldroyd-B extensional viscosity form. Overall, these studies take into account a number of additional factors, such as: finite extensibility, weakening of $\boldsymbol{N_1}$ effects, and balance of $\boldsymbol{N_1}$ and η_e influences.

Epd for Models A-D In Walters *et al.* [18], four constitutive Models A–D were introduced to investigate the influence of normal stress and extensional viscosity upon the *epd*-prediction, where Model-D represents Oldroyd-B and Model-A Newtonian (base-reference, with constant η_e). Model-B (*inelastic extensional*, $\boldsymbol{N_1}$=0) and Model C represent embellishments upon GNM1 and UCM1 models, respectively, from the work of Debbaut and Crochet [3] and Debbaut *et al.* [9]. Figure 3a conveys the corresponding findings on excess pressure drop (*epd*) against increasing deformation rate (*De*) for these four constitutive models (A-D). These data demonstrate the influence of the various rheometrical functions on *epd*-estimation. A comparison of Models-A to B shows the *increasing effect on epd* that extensional-viscosity has alone, as both models support vanishing $\boldsymbol{N_1}$. At the same time, under constant extensional viscosity (η_e), a comparison of Models-A to C indicates that increasing influence of normal stress difference can give rise to a *decrease* in *epd*, that is the opposite effect (as suggested in Binding [10].

Taking this comparison one step further, one may contrast *epd*-findings for Model-B ($\boldsymbol{N_1}$=0) versus Model-D (Oldroyd B). Note that, Oldroyd B reflects the same extensional viscosity as Model-B (an example of extreme strain-hardening), but Model-D has a non-zero normal stress-difference of quadratic variation in shear-rate (so, $\boldsymbol{N_1}\neq 0$). Model D is often used to approximate experimental results for Boger fluids, due to its constant shear-viscosity and strain-hardening properties. Consistent with the above, the results of Figure 3a again demonstrate decline in *epd* from Model-B to Model-D, and this may be associated with the consequent rise in $\boldsymbol{N_1}$. In addition, there is the usual upper-limit on *De* attainable in the simulations for Model-D (attributed to the unbounded nature of η_e). Here, there is a slight dip in *epd* before reaching the limiting value at the Newtonian reference line (for this level of solvent

fraction, β=0.9), which lies below the large positive *epd* experimental expectations reported for Boger fluids (Nigen and Walters [4]; Rothstein and McKinley [5, 1].

Following this line of approach, a direct comparison of Figure 3a *epd* results can be established for Models-C to D, both of which share in common the same quadratic $\boldsymbol{N_1}$ behaviour. Hence, this comparison is held useful to represents the effects of extensional viscosity alone (*nb.* Model-C bears a constant extensional viscosity). Once more, an increase is detected in *epd* from Model-C to that for Model-D, but now this finding may be attributed to rise in extensional viscosity.

Epd for α and J-models The α-Model and Oldroyd-B share the same extensional viscosity, with a constant shear viscosity. The choice α=1 reproduces Oldroyd-B first normal stress (Walters *et al.* [18]), and α=0 mimics the inelastic GNM1 model (see Debbaut and Crochet [3]). As such for the α-Model, the first normal stress difference (N_1) declines with reducing α-level. The relevant *epd* results are displayed in Figure 3b. Here the effect on *epd* of gradual N_1-weakening is apparent from the inelastic GNM1(α=0) to the Oldroyd-B(α=1) model; this may then be associated with the strong and sustained quadratic form of N_1 in the latter case of Oldroyd-B. The results for the inelastic model (α=0) show an increase in *epd*, initiated from the most early stages of deformation-rate rise. *Epd* results for Model-(α=0.1) take up a position interposed between the two extremes of α=0 and α=1, with *epd*-elevation above Oldroyd-B(α=1) and the Newtonian reference line, a finding that can be attributed to the reduction in N_1-influence from that of Oldroyd-B. Significantly, the maximum increase in *epd* for the α-Model lies at *De*=6.4, and even then substantiates only a modest 5% increase above the Newtonian *epd*-unity reference-line; a shift in the correct direction, but admittedly still far from the much more marked experimental findings. The viscometric (N_1) distinction of the J-Model is its sustained N_1-plateau levels attained at high deformation-rates (Figure 4a). Counterpart, *epd* predictions with the J-Model are given in Figure 3c. Here, the dependence on J-parameter level is clearly evident, with a trend in the direction anticipated, and positive *epd*-values for J sufficiently large. Unfortunately, J-Models suffer from the lack of finite extensibility along with Oldroyd-B, and with rise in J-level, the limiting *De* achievable reduces, so that the (J=1.0)-instance, provides the smallest such *De*–value

Epd for FENE-CR and generalised variants Our experience with these various forms of the FENE-CR model (capturing finite extensibility), is that they are indeed capable of predicting enhanced *epd*, unlike observations with Oldroyd-B alternatives. As observed in Figure 4a, the FENE CR model possesses a first-normal stress-difference weaker than the strong quadratic-form of Oldroyd-B, and strain-hardening gives way to a constant plateau in extensional viscosity (finite extensibility, Figure 4b). Elsewhere in Tamaddon-Jahromi *et al.* [20, 32], *epd* response has been examined for the FENE-CR(L=5) model in contrast to Oldroyd-B results (L=∞, constant η_s). There, the impact on *epd* has been established, from the extent of *lowering* of *epd* values due to η_e *damping*, and *elevation* due to N_1 *damping*. This knowledge has been gathered from solutions with L={3, 5, 10}. The evidence points to a clear trade-off between these two rheometric factors, with rising deformation-rate (or *De*). There is the additional positive benefit of limiting η_e-capping with the FENE-CR model, which provides access to a significantly wider range of *D*e-values than that reported for Oldroyd-B (limit *De*=5.1). Typically, FENE-CR predictions support upper limits of *De*~100 for L=3 (*epd* rise 5.2%), of *De*~70 for L=5 (*epd* rise 28%), of *De*~9 for

L=10 (*epd* rise 18%, see Figure 5). For L=10, the *epd*-trend at the upper *De*-limits is still rising, whilst for L=5 and 3 there is closer approximation to the limiting plateaux with $De \sim 10^2$. Thus, one observes an increase in *epd*-values for L=5 of 15% at *De*=10, and in the extended range up to *De*~70, this rises to approximately 28%. It has been shown more recently that this FENE-CR upper *De*-limit may still be further extended, up to say *De*~2000, with additional attention to discretisation improvements, as in improved centreline and continuity approximation, and switch in primary variable from stress to configuration tensor form [30)]. Thus, providing some 32% *epd*-enhancement. This is notably, still well short of experimental findings, in enhancement level and deformation-rate range. In the several decades beyond *De*=10, η_e is noted to approach its upper limiting-plateau, so that any further rise in *epd* can be unequivocally attributed to continual weakening of N_1 (from its quadratic form).

Furthermore, and based on the above finding, a new and generalised model FENE-CR(αJ^m) has been explored, combining features of FENE-CR, α-Model and J-Model. This model, supported theoretically with its still weaker form of first-normal stress-difference (N_1) in comparison to FENE-CR (Figure 4a), was devised to predict a considerably larger *epd*-enhancement (say, up to 200%, see Figure 5). Unfortunately, in practice this model inherits the poor numerical stability characteristics of its J-Model antecedent, due to the properties of its $\phi_2(\dot{\varepsilon})$ function and the roots of its denominator (see Table 1). As a consequence, all the above deliberations leave one disappointingly short of capturing the large positive *epd* experimental findings, reported for Boger fluids (Nigen and Walters [4]; Rothstein and McKinley [5, 1]). We proceed below to revisit this cycle of analysis, and overcome the barriers met above, by adopting alternative routes to solve the same problem.

5. Present numerical predictions versus experimental data

The *experimental* data for Boger fluids and the 4:1:4 geometry, as supplied by McKinley and co-workers (Rothstein and McKinley [5, 1]), is presented in Figure 6 (blue circle-line). Of considerable importance is the appearance of substantial increase in *epd* as the Deborah number rises. With respect to viscoelastic modelling, the wide discrepancy between numerical and experimental work has been suggested by some to relate to a missing dissipative contribution to the polymeric stress, arising from a *stress-conformation hysteresis* in the strong non-homogeneous extensional flow near the contraction plane. Rothstein and McKinley [5] cite Doyle *et al.* [33], Ryskin [34], and Rallison [35] on this issue. Rothstein and McKinley use this idea and pressure-drop data to derive an approximate powerlaw-type extensional viscosity, based on a Cogswell shear analysis [36], from which an approximate dissipative stress can be determined. The eWM_FENE-CR models employed in this work, hybrid extensional White Metzner and FENE-CR forms, achieve a similar objective, but transposed to the viscoelastic context, through the specification of its extensional viscosity function (see eWM_LPTT alternative in [20]). Such models naturally introduce an additional dissipative extensional-viscous time-scale (discussed above), and are based on a generalisation in complex flow for the strain-rate. The expectation for these models is to show a positive capacity to capture enhance levels of pressure drop, as desired.

5.1 ***Flow-rate (Q) increase solutions:*** swanINNFM(c), swanINNFM(q) models

In this section, we attempt to demonstrate the effective capture of enhance levels of pressure drop, discussing the necessary steps and procedure to adopt in achieving this goal. Following the split of solution approach into flow-rate increase and relaxation-time increase, first solutions are presented under consideration of increased flow-rate (*Q*) settings. Essentially, this involves ramping of the flow-rate between the various intermediate steady-state De-solutions attained. Here, Figure 6 conveys comparison of *epd* experimental data, of Rothstein and McKinley [1]), against the numerical predictions with the two dissipative model variants proposed - swanINNFM(c) and swanINNFM(q) models. As such, Figure 6a displays *epd* for the first variant (full-cosh), swanINNFM(c), with restriction for clarity to three values of dissipative extensional-viscous time-scale λ_D=0.1, 0.18, and 0.2. In this instance, one can observe that the *epd*(λ_D=0.1)-solution underestimates the experimental data, whilst the *epd*(λ_D=0.2)-solution provides overestimation. Hence, the *epd*(λ_D=0.18)-interpolant is seen to provide a close match to the experimental data, both in the mid-range 2.0≤*De*≤3.0 and in the earlier range 0≤*De*≤2.0. Beyond the *De*~3.0 level, the experimental data begins to attain its plateau (see below for discussion).

Figure 6b reflects a similar picture in experimental data capture with the alternative quadratic-approximation swanINNFM(q) model. In this form, solutions are displayed for $0 \le \lambda_D \le 0.26$, from which a tight window of capture is provided by the range $0.12 \le \lambda_D \le 0.16$. This provides the mid-range interpolant *epd*(λ_D=0.14), that well tracks the Rothstein and McKinley [1] *epd*-data right up to *De*~3.2+. One notes here, the slightly reduced demands on dissipative extensional-viscous time-scale λ_D -level to achieve such matching. Then, swanINNFM(q) solutions require only (λ_D=0.14), as opposed to (λ_D=0.18) with swanINNFM(c). Significantly, since inclusion of a larger dissipative factor is observed to affect numerical stability, hence this issue also influences *De*–solution levels for steady-state attenuation. Therefore, higher level *De*–solutions (with *epd*) may be achieved with the swanINNFM(q) option (more robust) than its full-cosh counterpart.

In Figure 6b, one may also note the location of the outer dashed limiting line, drawn to link the steady-solution limit-points observed for each instance of λ_D trialled. This effectively delimits the steady-unsteady transition boundary being mapped out.

Subsequently beyond *De*~3.2+, and to cover the wider range up to *De*=5.2+, the the Rothstein and McKinley [1] *epd*-data is better captured with λ_D-values in the reduced range of $0.1 \le \lambda_D < 0.14$. Yet, see below for further results in this extended rate range, when strain-rate capping is invoked.

Note, there is only a slight hint of an initial early-rate drop in *epd* (dip below unity-Newtonian reference-line, see below). This dip is itself a phenomenon that may be associated with stored energy and recoverable stress (Rothstein and McKinley, [1]), and seems to be a feature present when there is significant N_1 influence in the representation.

Moreover, extensional-viscosity capping (through restriction in strain-rate within the dissipative function $\phi(\dot{\varepsilon})$, to say, O(15) units) with either swanINNFM model options, is observed to resolve the limiting plateau the Rothstein and McKinley [1] *epd*-data behaviour. Such capped-results are shown in Figures 7(a-b), achieved beyond *De*=2.8 for the $\cosh(\lambda_D\dot{\varepsilon})$-form (Figure 7a), and *De*=3.2 for the quadratic-form (Figure 7b). It is particularly noteworthy that for the quadratic-option, to capture the experimental-*epd* between *De*=4 and *De*=5, capping levels must be reduced for a second-time, around *De*=4.1 to O(14) strain-rate units.

It is worth mentioning in passing, that experimentally and in some corresponding planar configurations, any excess pressure drop is not particularly prominent for Boger fluids ([4] for 32:1 and 20:0.5 contraction ratios). Clearly under planar deformation settings, the particular extensional viscosity model (swanINNFM(q)) advocated in this study theoretically collapses to the base FENE-CR form, through the definition of generalised strain-rate. Hence, since base FENE-CR axisymmetric solutions (say, with λ_D=0 of Figure 6b) under Q-increase provide considerably reduced *epd*, it follows that planar solutions will do so likewise. To illustrate this situation, one may compare data in Figure 6c under both planar and axisymmetric configurations, and within the deformation rate range $0 \le De^{Exp} \le 9$. Then, one can observe a significant decline in *epd* response between the axisymmetric (λ_D = 0, λ_D = 0.14) to the planar configuration (λ_D = 0)[‡]. Notably in the planar instance, there is an exaggerated early dip in *epd* over the axisymmetric case, to a minimum planar value of *epd*=0.964 at *De*~0.4, before reaching a delayed intercept with the unity reference line at *De*~1.4, and proceeding subsequently to an upper limit at *De*~9 of *epd*=1.16 (substantiating ultimate epd-enhancement, though admittedly modest). For the equivalent axisymmetric case with λ_D=0 (base FENE-CR), and at the same level of *De*=9, then *epd*=1.30, providing twice the epd-enhancement of its planar counterpart (though still relatively modest). Amongst the two axisymmetric results reported (λ_D = 0, λ_D = 0.14), the early dip in *epd* is seen to be increasingly suppressed as the dissipative time-constant is elevated.

5.2 Relaxation time **(λ_1)*-increase solutions:*** swanINNFM(c), swanINNFM(q) models

Subsequently, one turns to study the relaxation time (λ_1)-increase mode, whereupon Figure 8 illustrates *epd* counterpart solutions to the above, again with both swanINNFM model options. This is important to consider for back-reference, as one may note that all previous simulation results, covered and reported in section 4, were essentially reported under (λ_1)-increase mode. One observes that, under this mode of solution-approximation, the huge *epd*-enhancement of the experimental-*epd* may be captured once again with either model. That is with the proviso that now a suitable selection must be made over a ***set*** of extensional-viscous time-scales for λ_D. This requires a *different* λ_D*-value* for *each* λ_1*-increment* replacing the *single-value* of the *Q*-increase mode. With the $\cosh(\lambda_D\dot{\varepsilon})$-form, the λ_D-set is λ_D={0,…,4.0}; with the

[‡] Note, that the same average velocity in the constriction zone is taken as the basis of equitable comparison between axisymmetric and planar flows.

quadratic-option, the set is λ_D={0,…,3.5}. One observes that maxima in λ_D are now an order of magnitude greater than found under *Q*-increase mode, and the solution-lines at fixed-λ_D striate the *epd*-solution space. As such, their intercepts with the Rothstein and McKinley [1] *epd*-data provide the necessary characterisation anchor-points, from which to determine the λ_D–interpolant for each λ_1-value. In this manner, a cubic relationship may be recognized between dissipative extensional-viscous time-scale (λ_D) and fluid-relaxation time (λ_1) [red circle/line in Figure 8]. Once more to capture the Rothstein and McKinley [1] *epd*-data, as observed with the *Q*-increase mode above, a narrower range of λ_D (λ_D<3.5) is required with the quadratic-option in comparison to the $\cosh(\lambda_D\dot{\varepsilon})$-form ($\lambda_D$<4.0). Since lower-$\lambda_D$ requirement yields access to improved numerical stability and wider-*De* steady-state solution acquisition, hence only the quadratic-option is retained henceforth, in the analysis sections to follow.

5.3 Comparison of solutions: *Q-increase* versus λ_1-*increase*

Here, direct comparison is made between the solutions extracted with rising *De* and fixed λ_D =0.14, for the two possible solution approximation modes: of increasing flow-rate (*Q*-increase) and fluid-relaxation time increase (*λ_1-increase*). First, one gathers from Figure 9a, the large increase in *epd* and capture of the the Rothstein and McKinley [1] *epd*-data with flow-rate *Q*-increase. Second, and in contrast, the relatively unresponsive *epd*-solution line is noted under λ_1-increase, which asymptotes to a position parallel and above the unity-Newtonian reference-line, somewhat distant from the experimental data. As observed above from Figure 8b under λ_1-increase, *the relatively large value of λ_D =3.5 is necessary to capture extrema in the experimental data, almost 25 times larger than λ_D =0.14, as required under the Q-increase mode*. Thus, this considerable reduction in dissipative factor (and its fixed nature) renders the *Q*-increase mode the more robust and practical method to extract enhanced-*epd*.

In addition and in Figure 9b for λ_D=0.14, large vortex intensities are observed with *Q*-increase (*upstream, downstream*) in comparison to λ_1-increase (*upstream only*). Here, and for *De*={1, 3, 5}, enhancement in downstream vortex intensity with *Q*-increase is almost {10, 112, 1185} times larger than under λ_1-increase (static). Upstream vortex dynamics provides for vortex enhancement under both modes, so that for *De*={1, 3, 5}, factors of vortex intensity increase from λ_1-increase to *Q*-increase are now {10, 26, 47} times larger. Clearly here, the *Q*-increase mode generates considerably greater vortex activity. One notes in passing that, upstream vortex intensities for λ_1-increase and *Q*-increase at *De*=5 are $0.314*10^{1}$ and $14.7*10^{-1}$ respectively. The equivalent values in downstream vortex intensities are $0.004*10^{-1}$ and $4.74*10^{-1}$.

These significant differences in flow dynamics between Q-increase and λ_1-increase modes, expressed through *epd* and vortex intensity (Figure 9), are also clearly apparent in the rate of deformation fields of Figure 10. As anticipated under λ_1-

increase of Figure 10a, the maximum in strain-rate (of du_z/dz) remains unaltered (around 1.7 units), as *De* rises from *De*=1 to *De*=5. In contrast, *Q*-increase strain-rates show much larger levels. These lie around 8 times the 1.7 units value at *De*=1; reaching almost 96 times at *De*=5. Note under *Q*-increase and at *De*=1, that zones of small (dark blue) and large (red) strain-rates appear at the centreline and along the contraction-wall. There is an antisymmetric pattern detected about the centreline, large-positive-upstream to large-negative-downstream, with reflection about the obstruction plane. About the obstruction-cap, again the pattern is antisymmetric, but opposite in sign-direction upstream-downstream. These regions grow as elasticity rises, both upstream and downstream, becoming distorted, with larger extrema downstream. Strain-rate maxima near the obstruction-cap, compared with centreline values, are {2.2, 4.7, 5.6}-times larger for *De*={1, 3, 5}.

Similar growth trends are observed in shear-rate (du_z/dr) fields of Figure 10b. Here and under λ_1-increase, minima in shear-rate (Figure 10b) remain practically constant as *De* rises. Considering the counterpart *Q*-increase scenario (Figure 10b), significant differences are detected in shear-rate minima between solution states at *De*=1, 3, and 5. As *De* rises from *De*=1 to *De*=5, a growth zone of small (dark-blue) around the constriction is identified (see Figure 10b). For example, shear-rate minimum at *De*=1 is -50.93 units, shifting to -236.78 units at *De*=3; a factor of ~5 times. Between *De*=3 to *De*=5 solutions, the factor of increase is ~2 times (from -236.78 to -522.89 units). Here, the field patterns are generally symmetric about the obstruction-plane, upstream-downstream; becoming drawn slightly more upstream around the obstruction-cap as *De*–rises.

Additionally, this naturally leads on to charting corresponding first normal stress difference ($N_1=\tau_{zz}-\tau_{rr}$), as shown in fields Figure 10c (3D), and Figure 10d (2D) for both λ_1-increase and *Q*-increase modes. The 3D-plots are informative on relative growth of peak-values, their local nature and sharpness, and in contrast to their surroundings. The counterpart 2D-plots are also helpful, as the perspective-view in 3D-plots can obscure some of the important information to convey. In the complex flow situation, this contains both pure shear (boundary wall) and pure extensional (centreline) deformation regions, alongside mixed flow. Hence, earlier comments concerning increase-decrease in N_1 and extensional viscosity (η_e) from ideal homogeneous settings, and their relative impact on *epd*-estimation, can be reconsidered in this more general deformation context. Here, there is significant increase in N_1 under the *Q*-increase mode around the obstruction-wall. There, N_1-peak-values rise from N_1=37.8 units at *De*=1, to N_1=235.3 units at *De*=3, to N_1=814.1 units at *De*=5; which represents magnification of more than 20 times from *De*=1 to *De*=5. Note that, maxima in the first-normal stress (N_1) plots are located near the constriction mid-plane in shear, close to the constriction-cap around (r=1, z=0). In a similar fashion but in extension along the centreline, maxima in N_1 (representative of η_e) adjust through the *De*–rise as in: N_1=28.6 units at *De*=1, N_1=91.9 units at *De*=3, and N_1=150.1 units at *De*=5. This supports the expectation on η_e–enhancement of homogeneous flow. Notably, N_1 shear-maxima near the obstruction-cap, compared to N_1 extension-maxima along the centreline, are {1.3, 2.7, 5.4}-times larger alongside the rise in *De*={1, 3, 5}.

The situation is completely different in the λ_1-increase instance, where normal stress-maxima remain around the same order (O(4.8) units) as *De* rises. Hence, these

maxima are lower in magnitude from those for their *Q*-increase counterparts, by about a factor of nine at *D*e = 1.0 (maxima of 4.4 units) to some 50 times at *De* = 3.0 (maxima of 4.7 units). In addition, *Q*-increase data show an intense red-zone, of relatively large positive-values, which shifts upstream about the contraction with *De* rise. Such an increasing trend in N_1 does not emerge under the λ_1-increase scenario.

Furthermore, Figure 11 at *De*=5 provides 3D corresponding field plots for response in the dissipative function $\phi(\dot{\varepsilon})=1+\left(\lambda_D\dot{\varepsilon}\right)^2$. Here, the comparison of Figure 11a (λ_D=0.14) to Figure 11b (λ_D=3.5), under the increasing relaxation-time (λ_1-increase) mode, reveals there is significant increase in $\phi(\dot{\varepsilon})$ (of almost two order of magnitudes in extrema) around the constriction-cap and along the wall. The corresponding *epd=1.2* for λ_D=0.14, and *epd*=3.15 for λ_D=3.5 (see in Figure 11). This reflects almost 215% in *epd*-enhancement for λ_D=3.5, in comparison to only 20% *epd*-enhancement for λ_D=0.14. *One observes the crucial fact, that larger values of* $\phi(\dot{\varepsilon})$ *generate larger extensional viscosities in the non-homogeneous constriction flow-zone, resulting in corresponding epd–enhancement.* In addition, and with the smaller value of λ_D=0.14, even larger *epd*-values can be achieved under the increasing flow-rate (*Q*-increase) mode. This is demonstrated between Figures 11b and 11c, which manifests doubling in $\phi(\dot{\varepsilon})$ maxima, that provides *epd*-enhancement from 215% to 380% (now *epd*=4.8), an increase of some 165%. In this data, significant elevation is noted in the dissipative function $\phi(\dot{\varepsilon})=1+\left(\lambda_D\dot{\varepsilon}\right)^2$ as λ_D rises under *λ_1-increase*, and as elongation-rate rises under *Q-increase*. As such, dissipative extensional-viscous time-scale λ_D and elongation-rate $\dot{\varepsilon}$, are both factors that can provoke enhanced *epd*. Notably, the stronger influence of the two, proves to be through the elongation-rate factor.

5.4 Steady-oscillatory transition and flow instability

In Figure 12, three different flow phases (steady, oscillatory, and unstable) are identified against *De*-rise (*Q*-increase mode), for the quadratic-option swanINNFM(q) model with λ_D=0.14. Steady numerical solutions are predicted up to *De*=5. Then, oscillatory flow solutions appear at *De*~5.1, and are sustained throughout the range of 5.1≤*De*≤5.9. Subsequently, the flow becomes unstable, with solution divergence detected beyond *De*=5.9. In contrast, and reflecting on the experimental data of Rothstein & McKinley [1, 5], steady flow conditions are observed up to around *De*~2.8 (hollow symbols, Figure 12), beyond this point, the Rothstein and McKinley [1] *epd*-data level out, and subsequently, first oscillatory flow and then temporal instability is reported (filled symbols). These authors found that the onset of an elastic instability is first indicated by small amplitude oscillations in both the global pressure drop and the local velocity measurements which are observed to grow in magnitude with increasing Deborah number.

To further investigate the steady-oscillatory phase transition, Figure 13 displays the associated developments in total pressure-drop (Δp) across the contraction against time, for the base-value λ_D=0.14 and traced through *De*-rise. For *De*≤5, the pressure-drop is observed to be uniform in time, whilst oscillations onset (early in time) for De>5, becoming visually detectable in the double-magnification zoomed-view

(Figure 13b). The magnitude of these fluctuations increase with rise in *De*: showing first ordered oscillation at *De*=5.1 (constant amplitude-frequency); giving way to repeated regular-irregular fluctuation patterns at *De*=5.6; prior to more irregular-chaotic fluctuation patterns at *De*=5.9. Nevertheless, even at this advanced level of elasticity (*De*=5.9), such oscillatory behaviour in pressure-drop barely affects flow kinematics via the vortex structures generated (mimicking pseudo-steady form), see Figure 14 below. Conspicuously, pressure-drop gradually increases as *De* rises, generating values of $\Delta p=\{100, 650, 1900\}$ units at *De*={1, 3, 5}. Subsequently with $\lambda_D=0.14$, and between *De*=5.1 to *De*=5.9 solutions, there is almost 40-times increase in pressure-drop rising to $\Delta p=2800$ units.

Additionally, further evidence on temporal velocity development is displayed in Figure 14, now taken from two sample point locations, one around the inlet-centreline (Figure 14a), and another within the contraction-gap (Figure 14b). Data sampled from both locations provides evidence of smooth velocity solution form, as far as the peak-level of *De*=5.9 (see *De*=5.8 result). Only at this elevated level and within the contraction-gap location, is there any evidence of minor fluctuation in the kinematics. Moreover, to add supplementary solution evidence, the associated streamline patterns for three *De*-values, *De*={5.1, 5.6, 5.9}, are depicted in Figure 14c. From this, one notes that upstream vortex intensities are considerably larger in size compared to those downstream. For example at *De*=5.1, the upstream vortex (Ψ_{min}-value) is ~2.9 times larger than downstream, which by *De*=5.9, adjusts to a factor-difference of ~2.3 times.

Considering the impact on pressure-drop of elevation in λ_D, *in switching between* $\lambda_D=0.14$ to $\lambda_D=0.2$, then $\Delta p(\lambda_D=0.2)$ rises to around ~120% from *De*=3.7 ($\Delta p=1500$ units) to *De*=5.1 ($\Delta p=3300$ units), see Figure 15a. Hence, with the inclusion of a larger dissipative-factor of $\lambda_D=0.2$, the onset of oscillatory flow appears earlier, at around *De*=3.7, in comparison to *De*=5.1 with $\lambda_D=0.14$. Here with $\lambda_D=0.2$ solutions and for $De\leq3.5$, temporal solution development in pressure-drop is smooth and steady. For $De\geq3.5$ and with *De*-rise subsequently, both amplitude and frequency of fluctuations increase; fluctuation patterns become more irregular as the peak-vale of *De*=5.1 is approached. Figure 15b also provides the comparative streamline patterns for $0.1<De<5.1$ solutions. At the relatively low-level of *De*=0.1, both upstream and downstream vortex intensities maintain a balanced comparable size of $O(10^{-3})$. Once more with *De*-rise, upstream vortex intensity becomes much larger than for its downstream counterpart. Typically at *De*=3.5, upstream vortex intensity (Ψ_{min}) is ~2.87-times greater than that of the downstream vortex. At *De*=5.1, this upstream-downstream factor-difference approaches more like ~1.67-times.

5.5 Solution evolution and analysis of second eigenvalue (s_2) of stress-subsystem

In the various graphs provided in Figure 16, the second eigenvalue (s_2) of the stress-subsystem is seen to remain positive along the pure-extension centreline for all values of *De* noted. One notes here, the theory would indicate that $s_2=A_{zz}$ once $N_1<0$ along the centerline of the flow [30], and hence, negativity in the A_{zz} solution component in this zone should be avoided. The zoom insert on centreline A_{zz} data with *De*-rise, reveals the gradual decline in (s_2)-values and downstream shifts of its minima. Yet, positivity is maintained in this zone, and a lower limit would seem to apply.

It would appear, that even though the present simulation procedures use steady-state *De*-continuation (mimicking gradual flow-rate ramping experimentally, and do not evolve the Initial Value Problems (IVP) forward purely through time per *De*-solution), the hope is that any development of s_2-negativity in the field is kept to manageable levels, so that steady-solutions are still maintained. For example, under true time-evolution conditions, for a single *De*-solution (mimicking IVP theory) with sudden flow-rate ramping from *De*=0.1 state, experience dictates a steady critical De-solution state occurs around *De*~1.8, with divergence at *De*~1.9 (without any oscillatory flow phase detected). Under such conditions, s_2 does however remain positive in the field, through time evolution to steady-state for each *De*-solution level, as the IVP theory would demand.

Then, under *De*-continuation, a more detailed analysis of plots (3D & 2D) for the refined range $1.0 \leq De \leq 3.2$, seeks to locate more precisely the approach and onset of s_2-negativity. In the range $1.0 \leq De \leq 2.0$, s_2 is positive throughout the field ($s_{2min}>0$; s_{2min} represents s_2-global minimum in the field), although it follows a declining trend with *De*-rise, with only a slight hint of solution activity around the backface-tip of the contraction (3D-plot; Figure 17a, *De=1.0*). From this location, a light-blue fringe-contour level is growing, and by *De=2.0* (data not shown), this connects the constriction backface-tip region with the centreline, downstream of the contraction (2D-plots). Conspicuously, beyond such a stage and at *De=2.2* (Figure 17b), s_2-data enters negativity (s_{2min}=-0.08), localised about the constriction backface-tip. Tracing solution form from *De=2.8* ($-s_{2min}$=1.32; Figure 17c), the negative-peak based on the backface-wall is now accompanied by a second negative-peak (3D-plot), which appears behind the first-peak, yet less prominent. In the solution transition from *De*=2.8 to 3.0, and then 3.2 (the experimental range of some interest and comment; see Figure 17c-e respectively), one observes gradual growth of the first negative-peak, but with a sudden dramatic elevation occurring around *De*= 3.2 (as for *De=3.4*, see below).

Hence, and proceeding *beyond De=3.2*, steady predictive solutions are already displaying erratic nature. Rising to *De=3.4 (in the oscillatory experimental range; Figure 17f)*, the negative-peak based on the wall has grown some five-fold in intensity ($-s_{2min}$=7.32), and obscures the second negative-peak observed earlier in the *De*-rise. Here, the patch of negative s_2-values (strong blue) starts growing downstream and departs away from the contraction backface-wall (2D-plot). Elevating to *De=4.1 (Figure 18a)*, s_2-negativity slightly intensifies ($-s_{2min}$=7.86), but grows spatially, covering a significant region away from the contraction-wall (2D-plot). Various negative peaks are now apparent at *De=4.1*, all of them contained within the same region, accompanied with onset of upstream overshoot-undershoots and small red-positive peaks, alongside the relatively stronger blue-negative peaks (3D-plot). At *De=4.3 (Figure 18b)*, s_2-negativity reaches its extremum, with ($-s_{2min}$=14.56). Now there is a transfer of energy emerging between the two negative-peaks, with the second downstream-peak gradually increasing in strength. This position continues through solutions for *De*={4.5, 5.1, 5.9} *(see Figure 18c-e)*, whereupon smaller multiple ripple-peaks also appear. The overshoot-undershoot phenomena, with rising upstream red-positive peaks, is particularly prominent in solution for $5.1 \leq De \leq 5.9$ *(see Figure 18d-e)*, whilst approaching a state of numerical breakdown and solution intractability.

Effects of strain-rate capping This procedure significantly reduces the s_2-negativity for the same level of elasticity (as illustrated through De=3.4 solutions; contrast Figure 17f vs Figure 18f). The solution without-capping (Figure 17f) provides a pair of relatively more intense and sharper negative peaks ($-s_{2min}$=7.32). In contrast, with capping at the first-capped-level of *De*=3.4 (Figure 18f) and strain-rate constrained to less than 15 units, the global minimum is some five-times less intense ($-s_{2min}$=1.61). This reduction in s_2-negativity is sustained up to the second-capped-level of *De*=4.1, where stronger capping is enforced, with strain-rate constrained to less than 14 units. In this fashion, steady rheologically-constrained numerical solutions may be extended up to *De*=5.1 (with $-s_{2min}$=2.38), whilst faithfully tracking the *epd*-plateau levels displayed in the experimental results.

6. Conclusions

This study, motivated by much background work of many contributors, has attempted to capture numerically the highly elusive huge enhancements in pressure-drops observed experimentally for some Boger fluids in axisymmetric contraction-type flows, see Rothstein and McKinley [1]. To this end, a new dissipative model has been proposed for use in the simulation procedures with constant-shear viscosity, yet large extensional viscosity response. Such a model (motivated by Tamaddon-Jahromi *et al.* [19]) possesses an extension-rate dependent viscosity and is based on the combination of White-Metzner and FENE-CR constructions, providing a hybrid White-Metzner/FENE-CR model (swanINNFM). Notably, solutions with this model have successfully generated significant *epd* elevation, of over 200% above the Newtonian reference for these contraction-expansion flows.

This advance has only been made possible through a number of major strategies adopted. First, through constitutive model developments as discussed at length, and particularly to devise suitable and balanced rheometrical properties (in *N1 versus* η_e, see further comments below on this).

Second, it has been vital to identify the roll of problem approximation – seeking parity in experimental and simulation protocols over *epd*-assessment with rising *De*. Here, the importance of adopting the flow-rate increasing mode (*Q-increase, experimentally favoured*), as opposed to the mode through incrementation in fluid-relaxation time (λ_1*-increase, computationally favoured*), has been recognised and demonstrated. This demands scaling between experimental and simulation definitions in *De*, and ensures correlation on rate-ranges considered in either protocol. In this manner, it has been confirmed that flow-rate increase (*Q-increase*) conditions exhibit larger *epd*-enhancement, when compared to fluid-relaxation time increase (λ_1*-increase*), at the same level of dissipative extensional-viscous time-scale (λ_D).

Third, some new modelling strategies have been introduced, found particularly helpful in extraction of large *De*-solutions, and hence expanding the range of numerical solutions open to investigation. These strategies, discussed and referenced above, include: utilising the absolute value of the stress-trace function (*ABS-f*-correction); assuming the configuration tensor construct of the FENE-approach; adopting *fe/fv* improvements through advanced techniques in time discretisation, discrete treatment of pressure terms, velocity gradient treatment along the pure-

stretch flow-centreline (*VGR-correction*), correction for continuity, and compatible stress/velocity-gradient approximation.

Correspondingly, alongside large epd-enhancement, large vortex enhancement has been generated, both upstream and downstream with *De*-rise. Moreover, upon applying capping in the model through restriction in strain-rate, it is also practical to capture the limiting-plateau response noted in the experimental *epd*-data. Here, there is barely any initial decrease detected in *epd*, as associated with stored energy and recoverable stress, though this may be present in the very low range of deformation-rates (admittedly, not particularly explored in depth here).

Moreover, and for the quadratic-option swanINNFM(q) model in particular, it has now become possible to explore the different solution flow phases (steady, oscillatory, and unstable) identified against *De*-rise. In this respect, it has been shown that, the magnitude and chaotic form of fluctuation in pressure, rises with *De*-elevation, as there is transition between flow phases; these being of first steady solution, giving way to oscillatory form, before finally yielding to unstable, untractable and divergent form. Nevertheless, such oscillatory behaviour in pressure-drop has been observed to have very little impact upon the flow kinematics (mimicking pseudo-steady form), noted through the vortex structures generated.

In parallel with this work, a counterpart experimental-to-simulation study has also been conducted on the enhanced-drag past a falling-sphere (to appear separately). There comparable findings on an alternative flow problem have been developed (for generality of application – under different fluid solvent-fractions, deformation-settings and constriction-gap ratios), some of which have been found most instructive in exploring the many intricacies of the enhanced-*epd* theme. There also, close matching to experimental drag findings has been extracted, over comparable measures of deformation-rate between the experiments and the simulations.

There is still the intriguing question to address of *separation of elasticity* and *normal-stress* (and viscosity) *effects on pressure-drops*, which links arguments from viscometry to the *Linear Viscoelastic Regime* to complex flow response. This demands still further detailed investigation (beyond the scope of the present article), which requires splitting of the various component contributions to the total dissipation rate (itself related to *epd,* see Aguayo *et al*. [17]) to explain the source of the *epd*-enhancement, from the complex flow within the constriction window alone. In addition, this should be supported by the differences, detected across this complex flow zone, from idealised viscometric expectations (extensional viscosity and normal-stress) to those actually predicted by numerical solutions. Such theoretical and practical considerations are consigned to a further paper on '*epd* and a hyperbolic-shaped contraction-expansion geometric alternative' (Nyström *et al.* [37]).

On derivation of a physical understanding to this new swanINNFM *model* (with extension-rate dependent viscosity, constant in shear) - this may emerge from the background physics to substantiate the extensional dissipative response nurtured. So, for example, fibre suspension additives would point the way here to such a mechanism, providing dissipative extensional behaviour, and hence strong strain-hardening effects (yet little impact on shear properties). Since this concept may be applied under scale-reduction, at the mesoscopic-level to the molecular-level, one can

well see how appropriate physics may be constructed to substantiate such effects (applicable equally to planar deformation).

Concerning the modelling of Boger fluids, and the use of a more representative multi-mode as opposed to single-mode approximation (as used here), for its impact on present *epd*-findings - the use of such more realistic-fluid models would not change present *epd*-findings substantially. This is because the current modelling work attempts to distinguish differences associated with and boost *'hardening'* extensional viscosity behaviour alone (separability), by introducing extensional dissipative effects (inactive in shear), with its impact on pressure-drops. This position would not be substantially affected by a multi-mode approximation. Indeed, in Matallah *et al.* [38, 39], a detailed comparison was performed between a *'multi-mode'* and a *'single-mode'* approach, without fruitful outcome on enhanced pressure-drops and stress fields in complex flows. There, the key factor to estimating the pressure-drop accurately in complex flows was found to be the quality of fit to the shear viscosity, and in a single-mode case, reasonable qualitative correspondence was derived. Improved matching may be achieved to shear viscosity data with *'multi-mode'* approximation, but shear viscosity is essentially constant here anyway. Moreover, experience would dictate that, it is often found difficult to derive a good parameter match and fitting to both experimental shear and elongational data, simultaneously. Here, the incorporation of a dissipative extensional-viscous time-scale (λ_D), has proven to have a strong impact on dissipation with rising flow-rate, and it is this fact that is important to take advantage of (see also Rothstein & McKinley [1] on this point).

Acknowledgement
Sincere thanks must be expressed to the many helpful contributions made to this study through our colleagues in the INNFM Wales, but particularly to Professor Ken Walters FRS. I.E. Garduño (through scholarship No. 310618) and J. E. López-Aguilar would also like to gratefully acknowledge the financial support from Consejo Nacional de Ciencia y Tecnología (Mexico).

Dedication
This work has been written and dedicated to the memory of a dear sister-in-law, Linda Webster, recently deceased.

Appendix I*: Scaling factor on Deborah numbers: experimental versus numerical*

Standard experimental practice would provide for incrementation in an experimental Deborah number ($De_{\lambda_1}^{MIT} = De_{\lambda_1}^{Exp} = \lambda_1 Q/\left(\pi R_c^3\right)$) through raising the volume flow rate $Q\ \left(\mathrm{cm}^3/\mathrm{s}\right)$ at fixed geometric radius R_c and fluid relaxation time, λ_1. Experimentally, this approach proves convenient for retention of the same fluid across multiple flow-rate test runs (*Q*-increase). The relaxation time is based on values extracted from Rothstein and McKinley [1],

$$\lambda_1 = \frac{\text{first normal stress coefficient}}{2*\text{zero shear-rate viscosity}} = \frac{\Psi_{10}}{2\eta_0} = \frac{6.66\ \text{Pa s}^2}{2\left(22.75\ \text{Pa s}\right)} = 0.146\ \text{s}$$

In the simulations, a Deborah number ($De_{\lambda_1}^{Swan} = De_{\lambda_1}^{Sim} = \lambda_1 \bar{U}/\bar{L}$) is often stipulated, where $\bar{U}$ is a characteristic velocity (characteristic velocity across constriction) and $\bar{L}$ is a characteristic length (constriction width). In this form, common practice is to increment the simulation Deborah number ($De_{\lambda_1}^{Swan} = \lambda_1 \bar{U}/\bar{L}$) by raising the fluid relaxation time, λ_1, at fixed deformation rate, $\bar{U}/\bar{L}$ (λ_1*-increase*).

One may derive a relationship between these two definitions of Deborah number, experimental ($De_{\lambda_1}^{MIT} = De_{\lambda_1}^{Exp} = \lambda_1 \frac{Q}{\pi R_c^3}$) and computational ($De_{\lambda_1}^{Swan} = De_{\lambda_1}^{Sim} = \lambda_1 \bar{U}/\bar{L}$) and hence establish a scaling factor, in order to compare experimental and simulation findings on a one-to-one basis. Similar lines of argument for the *De*-simulation definition, and noting that the rate-factor $\left(\bar{U}/\bar{L}\right)$ is held fixed (which may be taken unambiguously as base-factor of unity), whilst varying (λ_1), then: $De_{\lambda_1}^{Swan} = \lambda_1 \frac{\bar{U}}{\bar{L}} = \lambda_1$.

As such, unity may also be established for $De_{\lambda_1}^{Swan}$ with a relaxation time setting of $\lambda_1^{sim} = 1\ \text{s}$.

On this basis, one may establish parity in common Group numbers, when one recognises the fixed factor in each definition. Hence, a scaling factor of $(1/\lambda_1^{exp})$ emerges, which yields:

$$De_{\lambda_1}^{Swan} = \frac{1}{0.146} De_{\lambda_1}^{MIT} = 6.8 De_{\lambda_1}^{MIT}.$$

Subsequently, once base parity has been established, the actual method of *De*-incrementation employed, experimentally or computationally, is of course open to selection in either setting.

Appendix II: **Approximations for the dissipation function**

The $\cosh(\lambda_D\dot{\varepsilon})$ function can be expanded into its constituent Taylor series components, viz.:

$$\cosh(\lambda_D\dot{\varepsilon}) = \frac{1}{2}\left\{e^{+\lambda_D\dot{\varepsilon}} + e^{-\lambda_D\dot{\varepsilon}}\right\}$$
$$= \frac{1}{2}\{1+\lambda_D\dot{\varepsilon}+(\lambda_D\dot{\varepsilon})^2+\ldots \quad \text{(II-1)}$$
$$1-\lambda_D\dot{\varepsilon}+(\lambda_D\dot{\varepsilon})^2-..\}.$$

Then successively, quadratic and quartic truncated approximations for $\phi(\dot{\varepsilon})=\cosh(\lambda_D\dot{\varepsilon})$ may be extracted, with even polynomial structure noted (as plotted in Fig. AII.1). Note that, the $\cosh(\lambda_D\dot{\varepsilon})$ and $[1+(\lambda_D\dot{\varepsilon})^2]$ functions intercept at around $\lambda_D\dot{\varepsilon}=2.9$, whilst the interception point between the $\cosh(\lambda_D\dot{\varepsilon})$ and $[1+(\lambda_D\dot{\varepsilon})^2+(\lambda_D\dot{\varepsilon})^4]$ functions is almost three times larger ($\lambda_D\dot{\varepsilon}=9.8$). Such forms (with linear in addition for comparison) have been used as appropriate replacement functions for ($\phi(\dot{\varepsilon})$), to overcome the rather over-strong exponential original form of $\cosh(\lambda_D\dot{\varepsilon})$ for $|\lambda_D\dot{\varepsilon}|\geq 3$, viz.:

$\phi(\dot{\varepsilon})\approx 1+\lambda_D\dot{\varepsilon}$ linear (II-2)

$\phi(\dot{\varepsilon})\approx 1+(\lambda_D\dot{\varepsilon})^2$ quadratic (II-3)

$\phi(\dot{\varepsilon})\approx 1+(\lambda_D\dot{\varepsilon})^2+(\lambda_D\dot{\varepsilon})^4$ quartic (II-4)

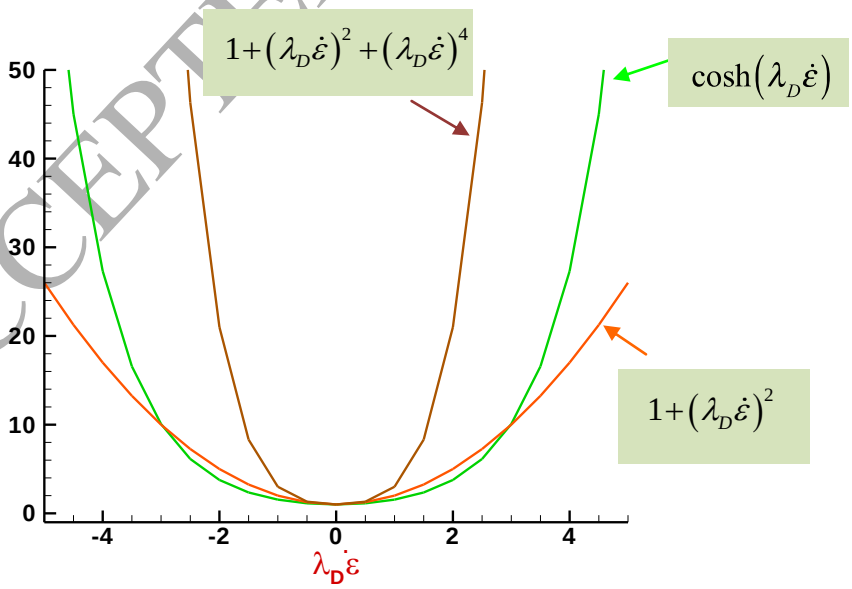

Figure AII.1 $\cosh(\lambda_D\dot{\varepsilon})$, quadratic $[1+(\lambda_D\dot{\varepsilon})^2]$ and quartic $[1+(\lambda_D\dot{\varepsilon})^2+(\lambda_D\dot{\varepsilon})^4]$ approximation functions

References

[1] J.P. Rothstein, G.H. McKinley, The axisymmetric contraction-expansion: the role of extensional rheology on vortex growth dynamics and the enhanced pressure drop, J. Non-Newton Fluid Mech. 98 (2001) 33-63.

[2] I.E. Garduño, H.R. Tamaddon-Jahromi, M.F. Webster, The falling sphere problem and capturing enhanced drag with Boger fluids, 2015, submitted to J. Non-Newton Fluid Mech.

[3] B. Debbaut, M.J. Crochet, Extensional effects in complex flows, J. Non-Newton Fluid Mech. 30 (1988) 169-184.

[4] S. Nigen, K. Walters, Viscoelastic contraction flows: comparison of axisymmetric and planar configurations, J. Non-Newton Fluid Mech. 102 (2002) 343-359.

[5] J.P. Rothstein, G.H. McKinley, Extensional flow of a polystyrene Boger fluid through a 4:1:4 axisymmetric contraction/expansion, J. Non-Newton Fluid Mech. 86 (1999) 61-88.

[6] L.E. Rodd, T.P. Scott, D.V. Boger, J.J. Cooper-White, G.H. McKinley, The inertio-elastic planar entry flow of low-viscosity elastic fluids in micro-fabricated geometries, J. Non-Newton Fluid Mech. 129 (2005) 1-22.

[7] D.V. Boger, A highly elastic constant-viscosity fluid, J. Non-Newton Fluid Mech. 3 (1977/1978) 87-91.

[8] M.G.N. Perera, K. Walters, Long range memory effects in flows involving abrupt changes in geometry. Part 1. Flows associated with L-shaped and T-shaped geometries, J. Non-Newton Fluid Mech. 2 (1977) 49-81.

[9] B. Debbaut, M.J. Crochet, H.A. Barnes, K. Walters, Extensional effects in inelastic liquids, Xth Inter. Congress on Rheology, Sydney (1988) 291-293.

[10] D.M. Binding, Further considerations of axisymmetric contraction flows. J. Non-Newton Fluid Mech. 41 (1991) 27-42.

[11] T.N. Phillips, A.J. Williams, Comparison of creeping and inertial flow of an Oldroyd B fluid through planar and axisymmetric contractions, J. Non-Newton Fluid Mech. 108 (2002) 25-47.

[12] M. Aboubacar, H. Matallah, H.R. Tamaddon-Jahromi, M.F. Webster, Numerical prediction of extensional flows in contraction geometries: hybrid finite volume/element method, J. Non-Newton Fluid Mech. 104 (2002) 125-164.

[13] K. Walters, M.F. Webster, The distinctive CFD challenges of computational rheology, Inter. J. for Numer. Meth. in Fluids 43 (2003) 577-596.

[14] Alves M.A., Oliveira P.J., Pinho F.T. (2004) On the effect of contraction ratio in viscoelastic flow through abrupt contractions, J. Non-Newton Fluid Mech. 122:117-130.

[15] D.M. Binding, P.M. Phillips, T.N. Phillips Contraction-expansion flows: The pressure drop and related issues, J. Non-Newton Fluid Mech. 137 (2006) 31-38.

[16] M. Pérez-Camacho, J.E. López-Aguilar, F. Calderas, O. Manero, M.F. Webster, Pressure-drop and kinematics of viscoelastic flow through an axisymmetric contraction–expansion geometry with various contraction-ratios, J. Non-Newton Fluid Mech. (2015).

[17] J.P. Aguayo, H.R. Tamaddon-Jahromi, M.F. Webster, Excess pressure-drop estimation in contraction flows for strain-hardening fluids, J. Non-Newton Fluid Mech. 153 (2008) 186-205.

[18] K. Walters, M.F. Webster, H.R. Tamaddon-Jahromi, The numerical simulation of some contraction flows of highly elastic liquids and their impact on the relevance of the Couette correction in extensional rheology, Chem. Eng. Sci. (2009), doi: 10,1016/j.ces.2009.01.007.

[19] H.R. Tamaddon-Jahromi, F.S. Syed, M.F. Webster, Studies on contraction flows and pressure-drops - extensional viscosity and dissipative stress effects, ICR Monterey, USA (2008) 1-3

[20] H.R. Tamaddon-Jahromi, M.F. Webster, K. Walters, Predicting numerically the large increases in extra pressure drop when Boger fluids flow through axisymmetric contractions, J. Natural. Science. 2 (2010) 1–11.

[21] Walters K., Webster M.F., Tamaddon-Jahromi H.R. The White-Metzner model Then and Now, Proceedings of the 25th Annual Meeting of the PPS meeting, Goa, India, IL 02 (2009) 1–14.

[22] M.D. Chilcott, J.M. Rallison, Creeping flow of dilute polymer solutions past cylinders and spheres, J. Non-Newton Fluid Mech. 29 (1988) 381-432.

[23] J.L. White, A.B. Metzner, Development of constitutive equations for polymeric melts and solutions, J. Appl. Polym. Sci. 7 (1963) 1867-1889.

[24] M.F. Webster, H.R. Tamaddon-Jahromi, M. Aboubacar, Time-Dependent Algorithms for Viscoelastic Flow: Finite Element/Volume Schemes, Numer. Meth. Par. Diff. Equ. 21 (2005) 272-296.

[25] H. Matallah, P. Townsend, M.F. Webster, Recovery and stress-splitting schemes for viscoelastic flows, J. Non-Newton Fluid Mech. 75 (1998) 139-166.

[26] J. Donea A Taylor-Galerking method for convective transport problems, Int. J. Numer. Methods Eng., 20 (1984) 101-119.

[27] O.C. Zienkiewicz, K. Morgan, J. Peraire, M. Vandati, R. Löhner, Finite elements for compressible gas flow and similar systems, Seventh International Conference on Computational Methods of Applied Science and Engineering (1985).

[28] P. Wapperom, M.F. Webster, A second-order hybrid finite-element/volume method for viscoelastic flows, J. Non-Newton Fluid Mech.79 (1998) 405-431.

[29] M. Aboubacar, H. Matallah, M.F. Webster, Highly elastic solutions for Oldroyd-B and Phan-Thien/Tanner fluids with a finite volume/element method: planar contraction flows, J. Non-Newton Fluid Mech. 103 (2002) 65–103.

[30] J.E. López-Aguilar, M.F. Webster, H.R. Tamaddon-Jahromi, O. Manero, High-Weissenberg predictions for micellar fluids in contraction–expansion flows, J. Non-Newton Fluid Mech. 222 (2015) 190–208, doi:10.1016/j.jnnfm.2014.11.008.

[31] P. Szabo, J.M. Rallison, E.J. Hinch, Start-up of flow of a FENE-fluid through 4:1:4 constriction in a tube, J. Non-Newton Fluid Mech. 72 (1997) 73-86.

[32] H.R. Tamaddon-Jahromi, M.F. Webster, P.R. Williams, Excess pressure drop and drag calculations for strain-hardening fluids with mild shear-thinning: Contraction and falling sphere problems, J. Non-Newton Fluid Mech. 166 (2011) 939–950, doi:10.1016/j.jnnfm.2011.04.009.

[33] P.S. Doyle, E.S.G. Shaqfeh, G.H. McKinley, S.H. Spiegelberg, Relaxation of dilute polymer solutions following extensional flow, J. Non-Newton Fluid Mech. 76 (1998) 79-110.

[34] G. Ryskin Calculation of the effect of polymer additive in a converging flow, J. Fluid Mech. 178 (1987) 423-440.

[35] J.M. Rallison, Dissipative stresses in dilute polymer solutions, J. Non-Newton Fluid Mech. 68 (1997) 61-83.

[36] F.N. Cogswell, Measuring the extensional rheology of polymer melts, Tran. Soc. Rheol., 16 (1972) 383-403.

[37] M. Nyström, H.R. Tamaddon Jahromi, M. Stading and M.F. Webster, Extracting extensional properties through excess pressure drop estimation in axisymmetric contraction and expansion flows for constant shear-viscosity, extension strain-hardening fluids, Rheol. Acta (2016) to appear.

[38] H. Matallah, P. Townsend, M.F. Webster, Viscoelastic multi-mode simulations of wire-coating, J. Non-Newton Fluid Mech. 90 (2000) 217-41.

[39] H. Matallah, P. Townsend, M.F. Webster, Computations of Polymeric Wire-coating Flows; Int. J. Numer. Methods Heat Fluid Flow 12(4) (2002) 404-33.

Figure captions

Table 1a. Constitutive models: Models B-D, α, J, α-J and FENE-CR(αJ^m), stress tensor forms
Table 1b. FENE-CR and swanINNFM models, conformation tensor forms
Table 2. Rheometrical functions, various models
Table3. Constitutive models, material properties and *epd* predictions
Figure 1. a) Schematic diagram, contraction-expansion geometry, b) zoomed mesh sections, 4:1:4 contraction/expansion: coarse (*elts=1080, nodes=2280, dof=14339, h-min=0.0099*), medium (*elts=1672, nodes=3519, dof=22038, h-min=0.0074*), refined (*elts=2112, nodes=4439, dof=27798, h-min=0.0058*)
Figure 2. Extensional viscosity of Oldroyd-B, FENE-CR; swanINNFM(c), swanINNFM(q) models, $\lambda_D = 0.1, 0.25, 4.0$
Figure 3. Normalised pressure-drop (*epd*) vs De, for a) A-D, b) α, and c) J models
Figure 4. Material function, a) first normal stress difference (N_1), b) Extensional viscosity (η_e) Oldroyd-B, α, J, FENE-CR, and FENE-CR(αJ^m) models
Figure 5. Normalised pressure-drop (*epd*) vs *De* for Oldroyd-B, J, FENE-CR, and FENE-CR(αJ^m) models
Figure 6. Normalised pressure-drop (*epd*) vs $De_{\lambda 1}^{Exp}$ for swanINNFM, a) $\cosh\left(\lambda_D \dot{\varepsilon}\right)$, b) $1+\left(\lambda_D \dot{\varepsilon}\right)^2$ models; c) planar vs axisymmetric, $1+\left(\lambda_D \dot{\varepsilon}\right)^2$ model
Figure 7. Normalised pressure-drop (*epd*) vs $De_{\lambda 1}^{Exp}$ for swanINNFM, a) $\cosh\left(\lambda_D \dot{\varepsilon}\right)$, b) $1+\left(\lambda_D \dot{\varepsilon}\right)^2$ models, flow-rate (*Q*) increase, finite plateau cap
Figure 8. Normalised pressure-drop (*epd*) vs $De_{\lambda 1}^{Exp}$ for swanINNFM, a) $\cosh\left(\lambda_D \dot{\varepsilon}\right)$, b) $1+\left(\lambda_D \dot{\varepsilon}\right)^2$ models, λ_1- increase
Figure 9. a) Normalised pressure-drop (*epd*) vs $De_{\lambda 1}^{Exp}$, b) stream function, λ_1-increase vs *Q*-increase, swanINNFM(q) model, λ_D=0.14, Ψ_{min}= -Ψ^*_{min}*10^{-1}
Figure 10. a) strain-rate b) shear-rate fields c, d) 3D, 2D first normal stress difference (N_1), λ_1-increase vs *Q*-increase, swanINNFM(q) model, λ_D=0.14
Figure 11. $\phi(\dot{\varepsilon})=1+\left(\lambda_D \dot{\varepsilon}\right)^2$, a, b) λ_1-increase (λ_D=0.14 and 3.5), c) *Q*-increase (λ_D=0.14)
Figure 12. Normalised pressure-drop (*epd*) vs $De_{\lambda 1}^{Exp}$ for swanINNFM(q) model, flow-rate (*Q*) increase, λ_D=0.14, full symbols represent oscillatory flow condition
Figure 13. Temporal pressure-drop across contraction, λ_D=0.14: rising-*De*, swanINNFM(q)], *Q*-increase; a) full view, b) zoomed view
Figure 14. Temporal velocity development, λ_D=0.14: a) inlet centreline b) contraction zone; c) stream function (Ψ_{min}= -Ψ^*_{min}*10^{-1}); rising-*De*, swanINNFM(q), *Q*-increase
Figure 15. a) Temporal pressure-drop across contraction, b) stream function (Ψ_{min}= -Ψ^*_{min}*10^{-1}); rising-*De*, swanINNFM(q), λ_D=0.2, *Q*-increase
Figure 16. a) A_{zz} & b) N_1 *@ centreline* against rising-*De*, λ_D=0.14; swanINNFM(q), *Q*-increase
Figure 17. s_2-tracking, λ_D=0.14; No-capping strategy against rising-*De* ($1.0 \le De \le 3.4$); swanINNFM(q), *Q*-increase
Figure 18. s_2-tracking, λ_D=0.14; a)-e): No-capping strategy against rising-*De* ($4.1 \le De \le 5.9$); f) Capping-strategy @ *De*=3.4; swanINNFM(q), *Q*-increase
Figure AII.1 $\cosh\left(\lambda_D \dot{\varepsilon}\right)$, quadratic $[1+\left(\lambda_D \dot{\varepsilon}\right)^2]$ and quartic $[1+\left(\lambda_D \dot{\varepsilon}\right)^2+\left(\lambda_D \dot{\varepsilon}\right)^4]$ approximation functions

Table 1a. . Constitutive models: Models B-D, α, J, α-J and FENE-CR(αJ^m), stress tensor forms

$$f\boldsymbol{\tau} + De\,\phi_1(\dot{\gamma})\,\overset{\nabla}{\boldsymbol{\tau}} = 2(1-\beta_{\text{Solvent}})\,\phi_2(\dot{\varepsilon})\,f\,\mathbf{d}, \text{ where,}$$

Models	$\phi_1(\dot{\gamma})$	$\phi_2(\dot{\varepsilon})$	$\phi_3(\dot{\varepsilon})$	f
B model	--	$\left(\frac{1}{1-De\dot{\varepsilon}-2(De\dot{\varepsilon})^2}\right)$	--	1
C model	1	$\left(1-De\dot{\varepsilon}-2(De\dot{\varepsilon})^2\right)$	--	1
Oldroyd-B (D model)	1	1	--	1
α model	α	$\left[\frac{1-\alpha De\dot{\varepsilon}-2\alpha^2De^2\dot{\varepsilon}^2}{1-De\dot{\varepsilon}-2De^2\dot{\varepsilon}^2}\right]$, $0\le\alpha\le 1.0$	--	1
J model	$\left[\frac{1}{1+J\dot{\gamma}^2}\right]$	$\frac{1-De\phi_3(\dot{\varepsilon})\dot{\varepsilon}-2De^2\phi_3^2(\dot{\varepsilon})\dot{\varepsilon}^2}{1-De\dot{\varepsilon}-2De^2\dot{\varepsilon}^2}$	$\frac{1}{1+3J\dot{\varepsilon}^2}$, $J\ge 0$	1
α - J model	$\alpha\left[\frac{1}{1+J\dot{\gamma}^2}\right]$	$\frac{1-De\alpha\phi_3(\dot{\varepsilon})\dot{\varepsilon}-2De^2\alpha^2\phi_3^2(\dot{\varepsilon})\dot{\varepsilon}^2}{1-De\dot{\varepsilon}-2De^2\dot{\varepsilon}^2}$, $0\le\alpha\le 1.0$	$\left[\frac{1}{1+3J\dot{\varepsilon}^2}\right]$, $J\ge 0$	1
FENE-CR(αJ^m)	$\alpha\left[\frac{1}{1+J\dot{\gamma}^m}\right]$, $0\le m\le 2$	$\frac{f_{\text{Fene}}^2-f_{\text{Fene}}\,De\alpha\phi_3(\dot{\varepsilon})\dot{\varepsilon}-2De^2\alpha^2\phi_3^2(\dot{\varepsilon})\dot{\varepsilon}^2}{f_{\text{Fene}}^2-f_{\text{Fene}}\,De\dot{\varepsilon}-2De^2\dot{\varepsilon}^2}$, $0\le\alpha\le 1.0$	$\frac{1}{1+3J\dot{\varepsilon}^m}$, $J\ge 0$	$\frac{L^2+[De/(1-\beta)]\text{Tr}(\boldsymbol{\tau})}{L^2-3}$

Table 1b. FENE-CR and swanINNFM models, conformation tensor forms

$$\boldsymbol{T} = \frac{(1-\beta)}{\text{De}}\,f\left[\text{Tr}(\mathbf{A})\right]\mathbf{A}\phi(\dot{\varepsilon}) + 2\beta\phi(\dot{\varepsilon})\mathbf{d}, \qquad \text{De}\,\overset{\nabla}{\mathbf{A}} + f\left[\text{Tr}(\mathbf{A})\right](\mathbf{A}-\text{I}) = 0, \text{ where}$$

Models	$\phi(\dot{\varepsilon})$	f
FENE-CR	1	$\frac{1}{1-\text{Tr}(\mathbf{A})/L^2}$
swanINNFM	$\cosh\left(\lambda_D\dot{\varepsilon}\right)$ or $1+\left(\lambda_D\dot{\varepsilon}\right)^2$	$\frac{1}{1-\text{Tr}(\mathbf{A})/L^2}$

Table 2. Rheometrical functions, various models

Models	η	η_e	N_1
A (Newtonian)	η_0	$3\eta_0$	0
B (Generalised Newtonian)	η_0	$3\beta_{solvent}\eta_0 + 3(1-\beta_{solvent})\eta_0\left[\frac{1}{1-De\dot{\varepsilon}-2De^2\dot{\varepsilon}^2}\right]$	0
C (White-Metzner)	η_0	$3\eta_0$	$2\eta_0(1-\beta_{solvent})De\dot{\gamma}^2$
D (Oldroyd-B)	η_0	$3\beta_{solvent}\eta_0 + 3(1-\beta_{solvent})\eta_0\left[\frac{1}{1-De\dot{\varepsilon}-2De^2\dot{\varepsilon}^2}\right]$	$2\eta_0(1-\beta_{solvent})De\dot{\gamma}^2$
α (White-Metzner)	η_0	$3\beta_{solvent}\eta_0 + 3(1-\beta_{solvent})\eta_0\left[\frac{1}{1-De\dot{\varepsilon}-2De^2\dot{\varepsilon}^2}\right]$	$2\eta_0(1-\beta_{solvent})\alpha De\dot{\gamma}^2$ $0\le\alpha\le1.0$
J (White-Metzner)	η_0	$3\beta_{solvent}\eta_0 + 3(1-\beta_{solvent})\eta_0\left[\frac{1}{1-De\dot{\varepsilon}-2De^2\dot{\varepsilon}^2}\right]$	$\frac{2\eta_0(1-\beta_{solvent})De\dot{\gamma}^2}{1+J\dot{\gamma}^2}$ $0\le J\le1.0$
FENE-CR	η_0	$3\beta_{solvent}\eta_0 + 3(1-\beta_{solvent})\eta_0\left[\frac{f_{Fene}^2}{f_{Fene}^2-f_{Fene}De\dot{\varepsilon}-2De^2\dot{\varepsilon}^2}\right]$	$\frac{2\eta_0(1-\beta_{solvent})De\dot{\gamma}^2}{f_{Fene}^2}$
FENE-CR(αJ^m)	η_0	$3\beta_{solvent}\eta_0 + 3(1-\beta_{solvent})\eta_0\left[\frac{f_{Fene}^2}{f_{Fene}^2-f_{Fene}De\dot{\varepsilon}-2De^2\dot{\varepsilon}^2}\right]$	$\frac{2\eta_0(1-\beta_{solvent})\alpha De\dot{\gamma}^2}{(1+J\dot{\gamma}^m)f_{Fene}^2}$, $0\le m\le 2$
swanINNFM	η_0	$3\beta_{solvent}\phi(\dot{\varepsilon})\eta_0 + 3(1-\beta_{solvent})\phi(\dot{\varepsilon})\eta_0\left[\frac{f_{Fene}^2}{f_{Fene}^2-f_{Fene}De\dot{\varepsilon}-2De^2\dot{\varepsilon}^2}\right]$, $\phi(\dot{\varepsilon})$ defined in Table 1b	$\frac{2\eta_0(1-\beta_{solvent})De\dot{\gamma}^2}{f_{Fene}^2}$

Table3. Constitutive models, material properties and *epd* predictions

Models	**Material properties**	**Critical *De***	***epd* enhancement**
B (Generalised Newtonian)	**ηe** same as Old_B; **ηs** const; **N1**=0	**0.6**	**8%**
C (White-Metzner)	(**ηe** , **ηs**) const; **N1 - damping**	**2**	*epd* decreasing
D (Oldroyd-B)	**ηe** extreme strain hardening; **ηs** const; **N1=quadratic**	**5**	**1%**
α (White-Metzner)	**ηe** same as Old_B, **ηs** const, **N1=weaker than Old-B**	**(α=0.1) 6.4**	**5%**
J (Whit-Metzner)	**ηe** same as Old_B; **ηs** const; **N1 - damping (J=0, Oldroyd-B)**	**1 (J=1) 3 (J=0.01)**	**5%** *epd* decreasing
α - J (Whit-Metzner)	**ηe** same as Old_B; **ηs** const; **N1 - damping**	**(α=0.1, J=1) 0.5**	**5%**
LPTT	**ηe** same as Old_B(Capped); **ηs** shear-thinning **N1 - damping**	**4 (ε=0.4) 8 (ε=4*10-4)**	*epd* decreasing *epd* decreasing / increasing below Newtonian ref. line
FENE-CR(L=5)	η_e same as Old_B(Capped); η_s const; **N1 - damping**	**70 (L=10) 9**	**28% 18%**
FENE-CR(L=5) abs(f), continuity correction	η_e same as Old_B(Capped); η_s const; **N1 - damping**	**2000**	**32%**
FENE-CR(L=5) abs(f),continuity/ VGR correctios	**ηe** same as Old_B(Capped); **ηs** const; **N1 - damping**	**3400 (L=10) 19**	**35% 47%**
swanINNFM(c) (L=5)	**ηe** WM[(**cos($\lambda_D\dot{\varepsilon}$)**)]_FENE-CR; **ηs** const; **N1 – damping**	**O(30-40)**	**~ 200% Matching Exp.**
swanINNFM(q) (L=5)	**ηe** WM[(**1+ ($\lambda_D\dot{\varepsilon}$)^2**)]_FENE-CR; **ηs** const; **N1 – damping**	**O(30-40)**	**~ 200% Matching Exp.**

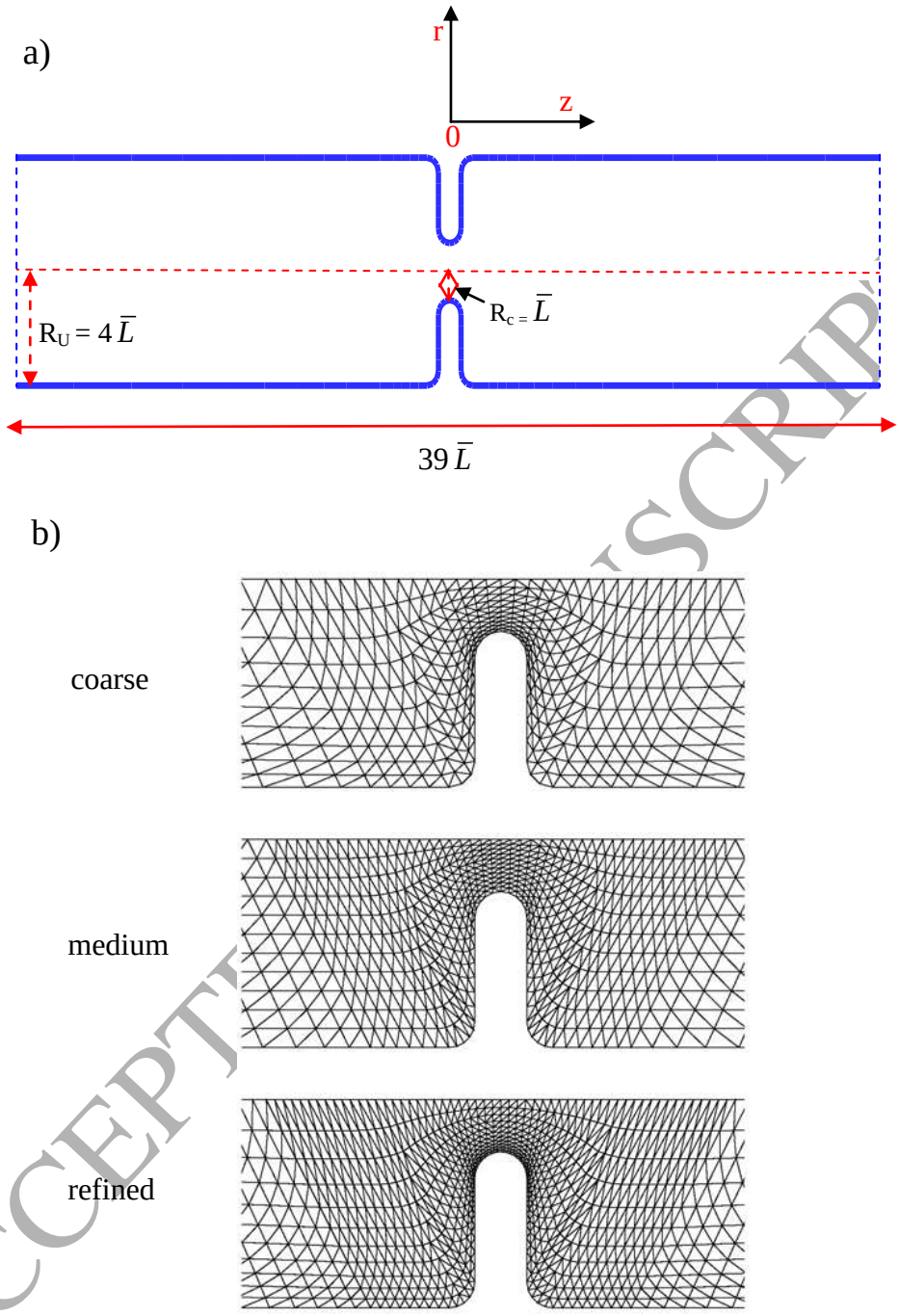

Figure 1. a) Schematic diagram, contraction-expansion geometry, b) zoomed mesh sections of 4:1:4 contraction/expansion: coarse (*elts=1080, nodes=2280, dof=14339, h-min=0.0099*), medium (*elts=1672, nodes=3519, dof=22038, h-min=0.0074*), and refined (*elts=2112, nodes=4439, dof=27798, h-min=0.0058*)

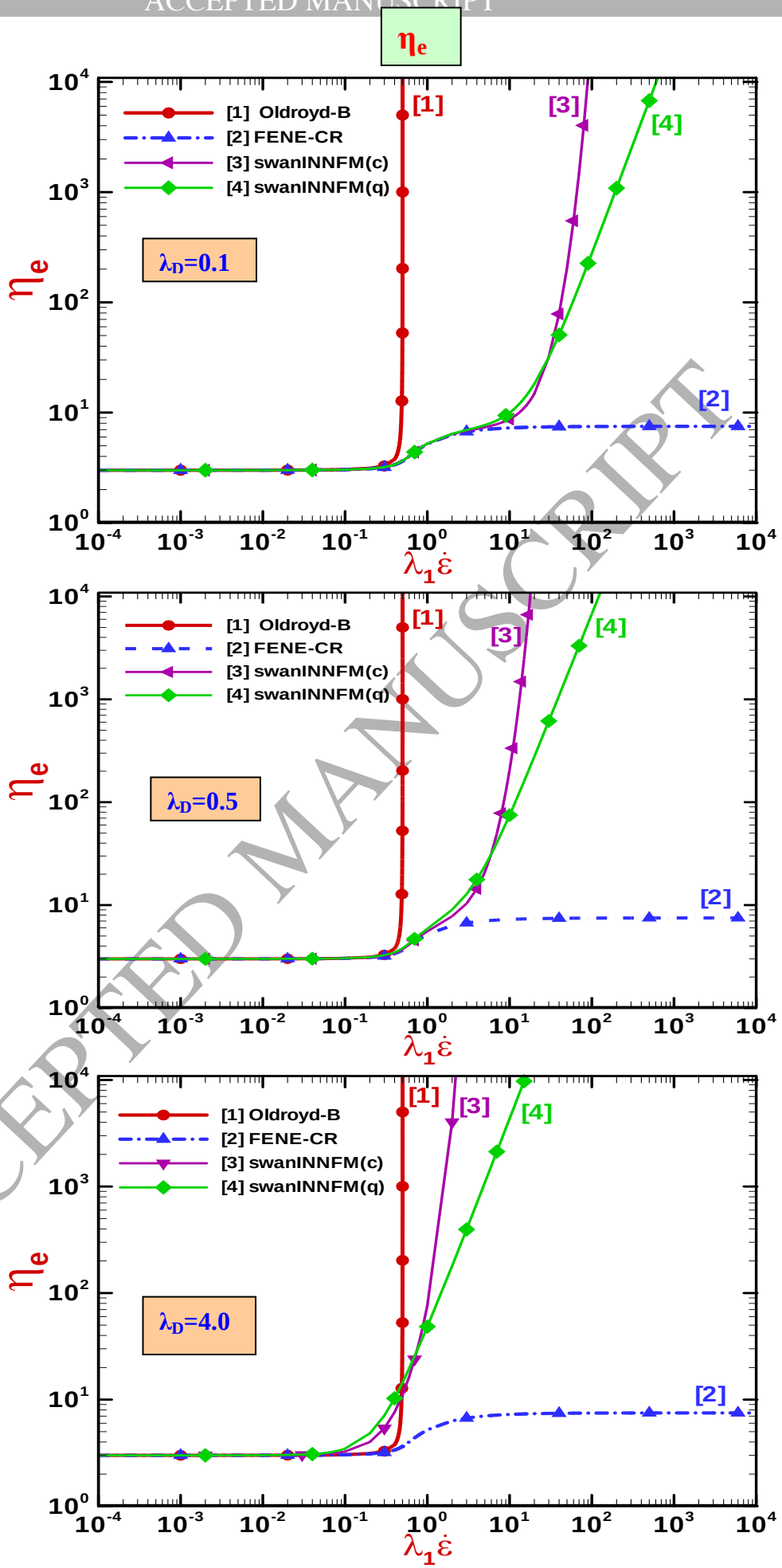

Figure 2. Extensional viscosity of Oldroyd-B, FENE-CR; swanINNFM(c), swanINNFM(q) models, $\lambda_D = 0.1, 0.25, 4.0$

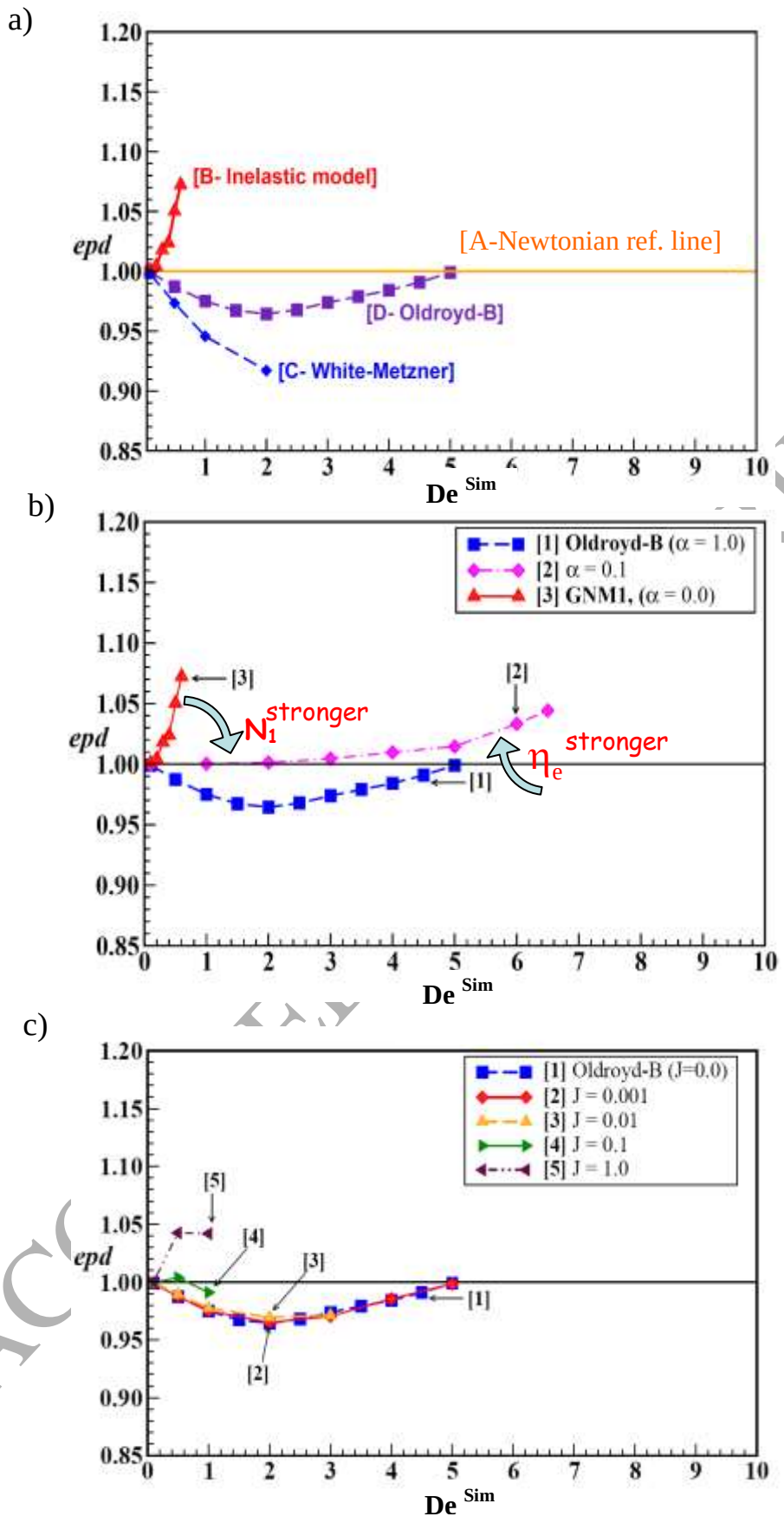

Figure 3. Normalised pressure-drop (*epd*) vs De , for a) A-D, b) α, and c) J models

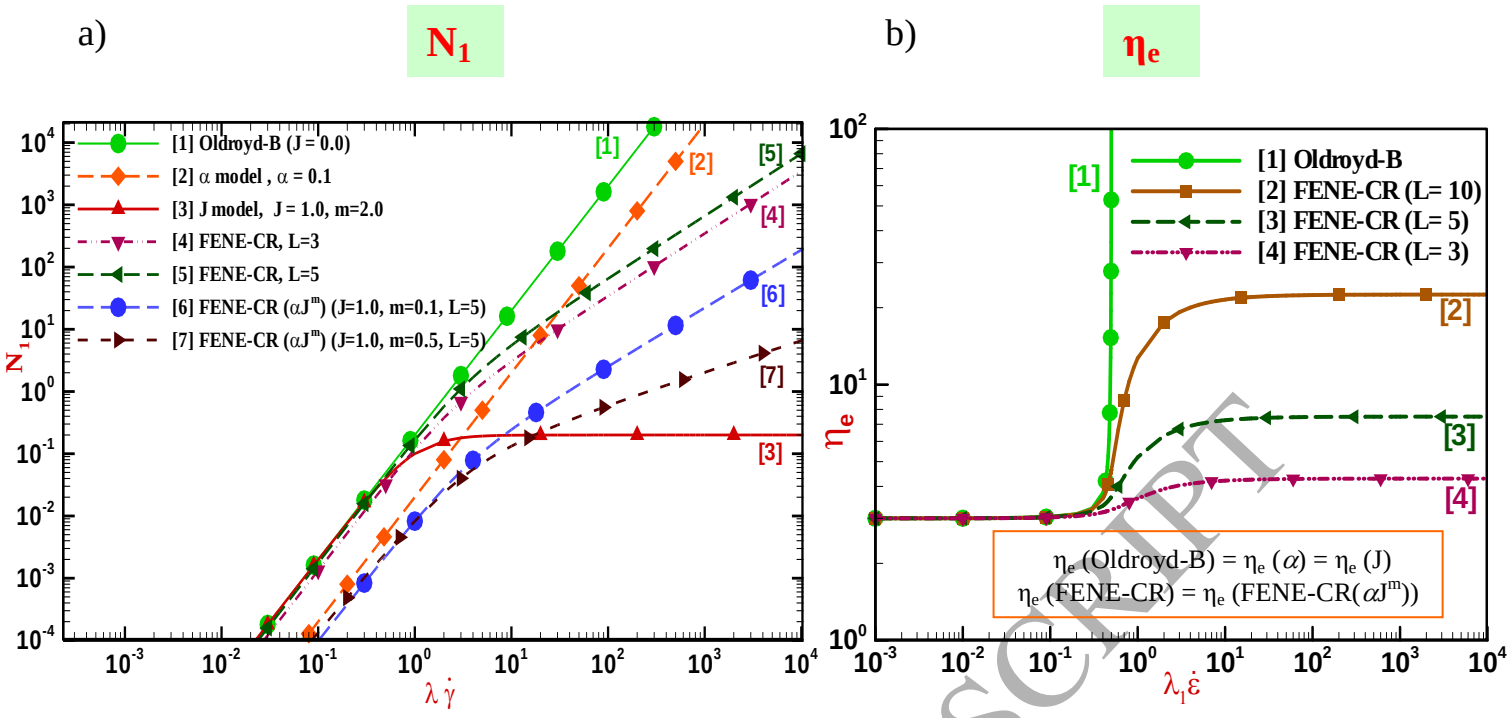

Figure 4. Material function, a) first normal stress difference (N_1), b) Extensional viscosity (η_e) Oldroyd-B, α, J, FENE-CR, and FENE-CR(αJ^m) models

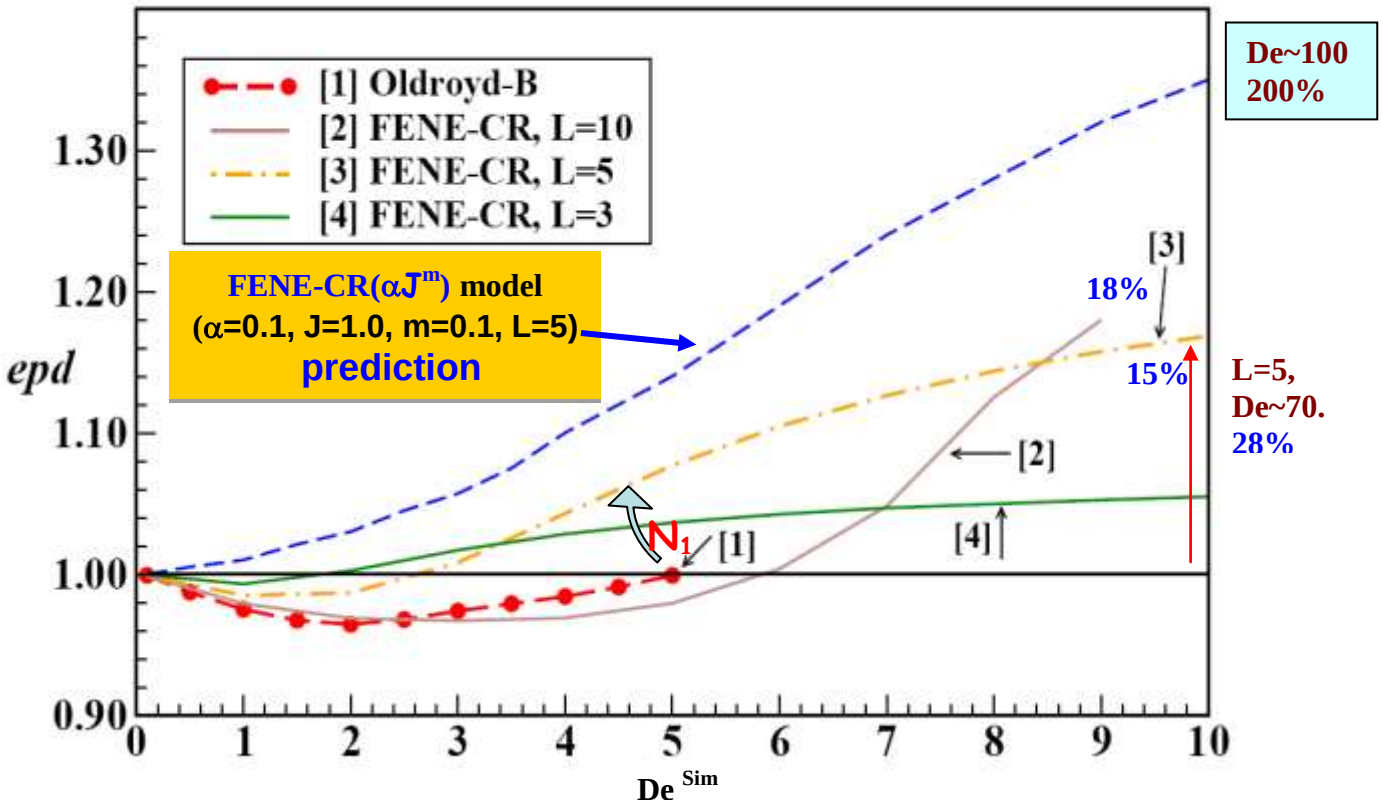

Figure 5. Normalised pressure-drop (*epd*) vs *De* for Oldroyd-B, J, FENE-CR, and FENE-CR(αJ^m) models

Q-increase

a)

[Cosh($\lambda_D \dot{\varepsilon}$)]

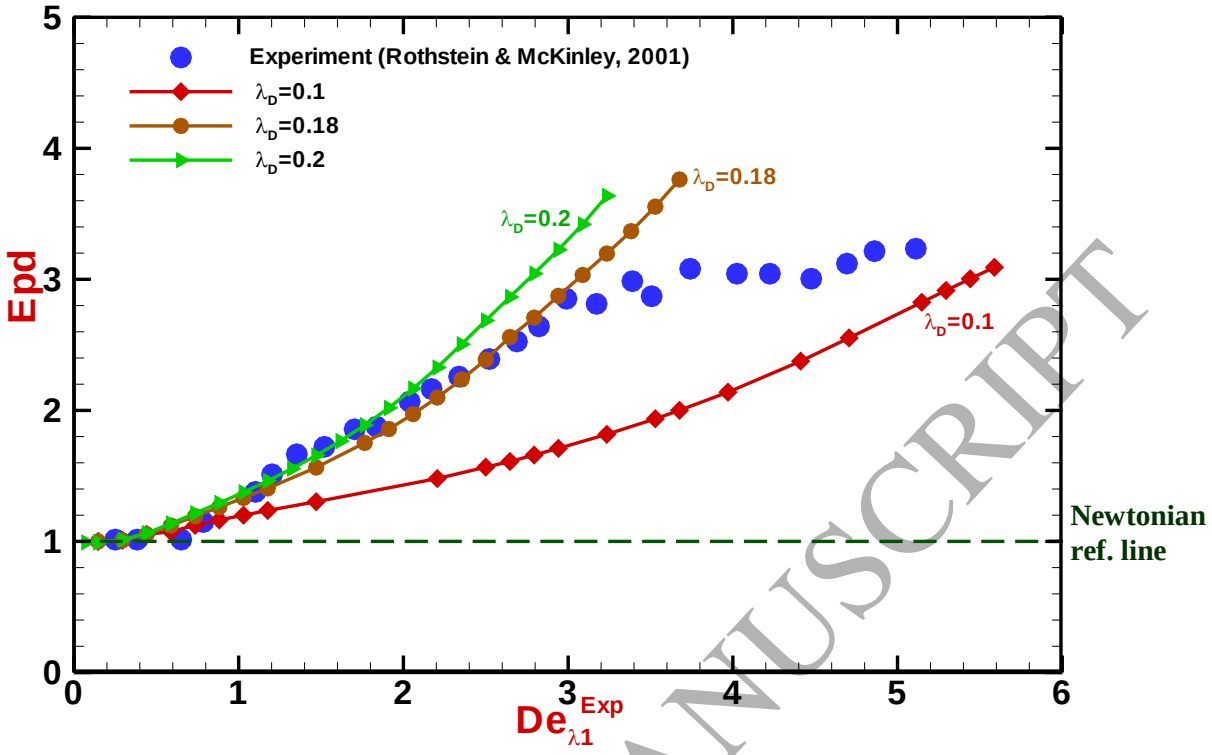

b)

[$1+\left(\lambda_D \dot{\varepsilon}\right)^2$]

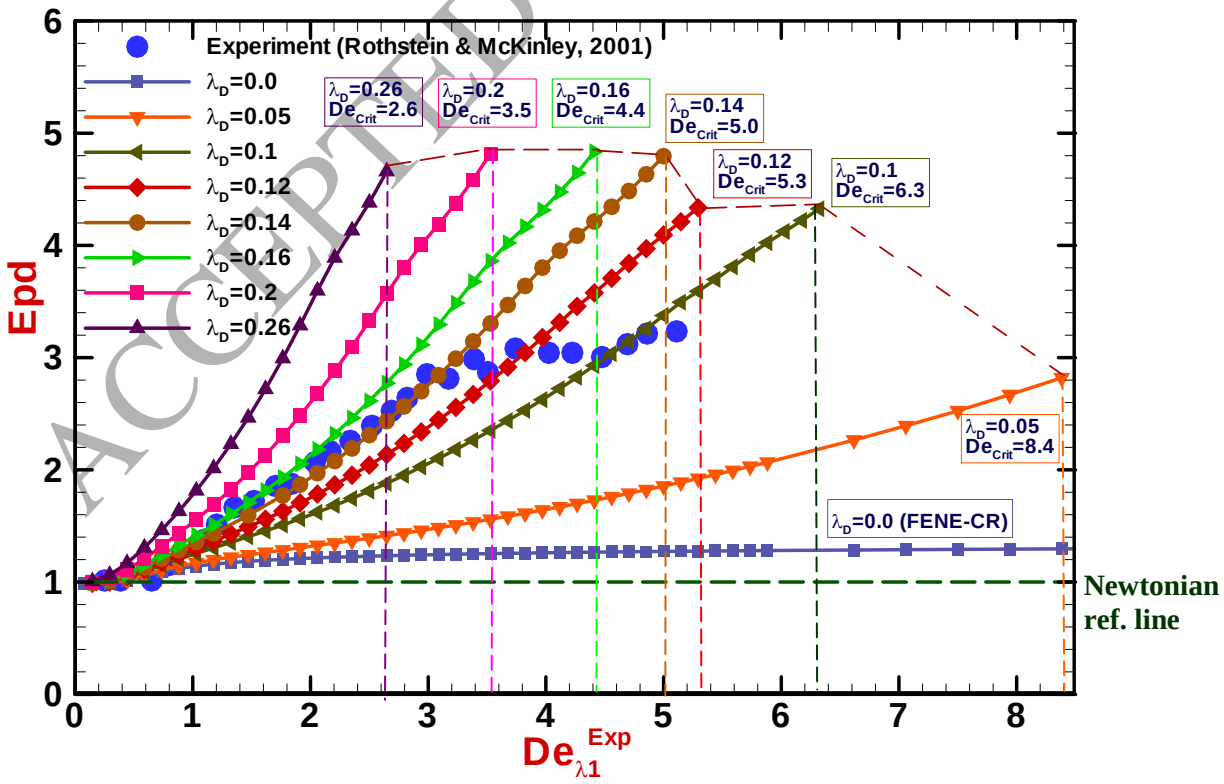

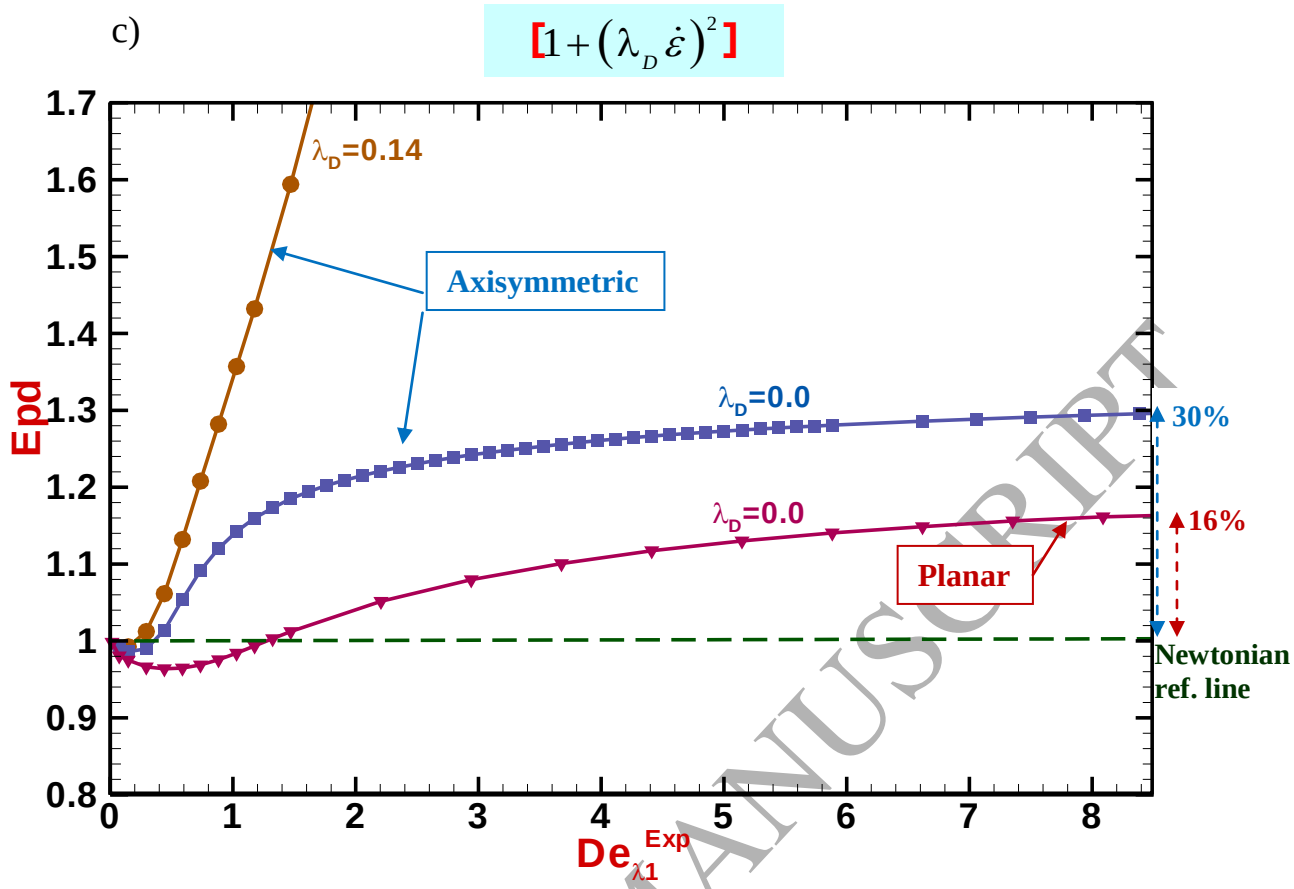

Figure 6. Normalised pressure-drop (*epd*) vs $De^{Exp}_{\lambda 1}$ for swanINNFM, a) $\cosh(\lambda_D\dot{\varepsilon})$, b) $1+(\lambda_D\dot{\varepsilon})^2$ models; c) planar vs axisymmetric, $1+(\lambda_D\dot{\varepsilon})^2$ model

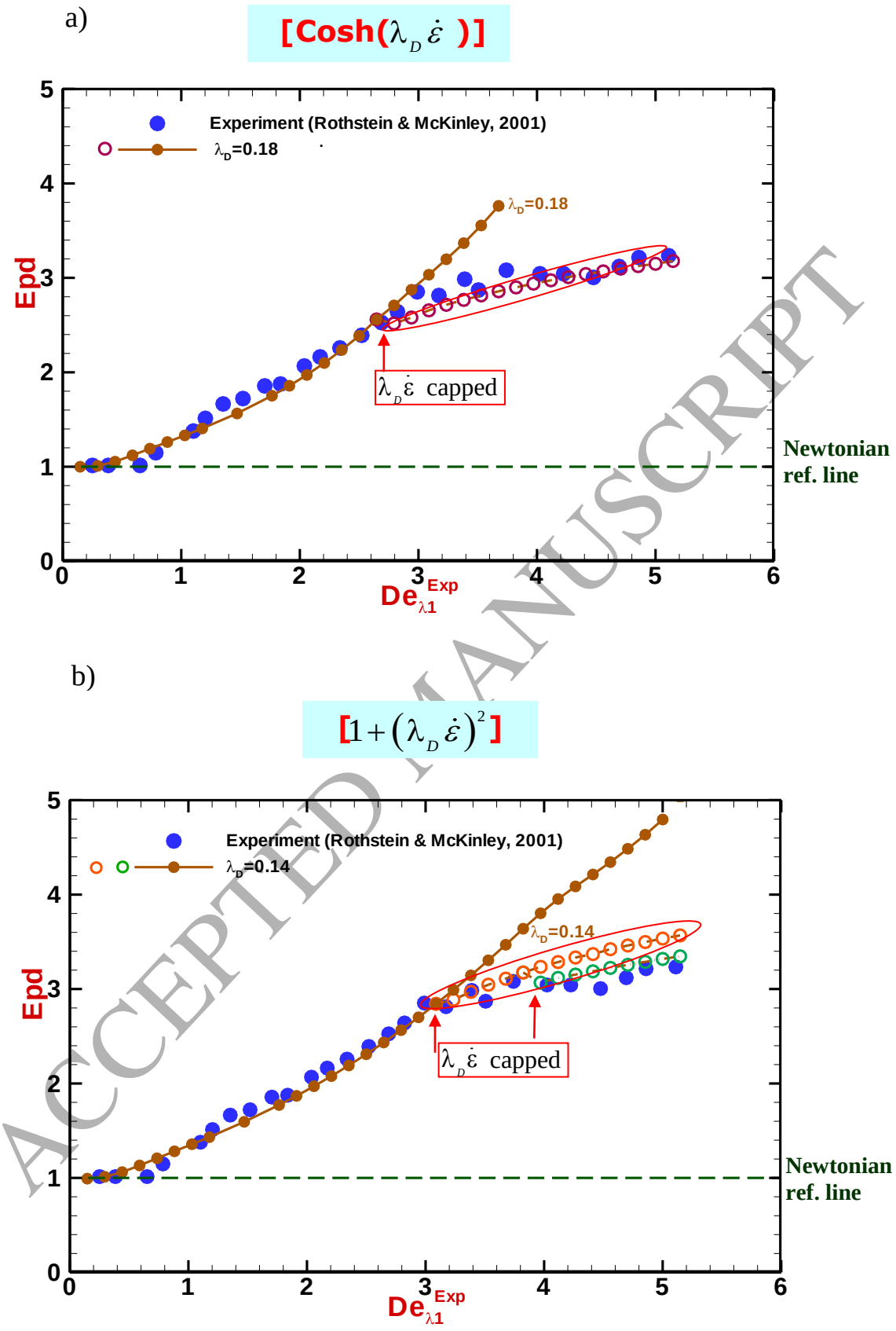

Figure 7. Normalised pressure-drop (*epd*) vs $De_{\lambda 1}^{Exp}$ for swanINNFM, a) $\cosh\left(\lambda_D \dot{\varepsilon}\right)$, b) $1+\left(\lambda_D \dot{\varepsilon}\right)^2$ models, flow-rate (Q) increase, finite plateau cap

λ_1- increase

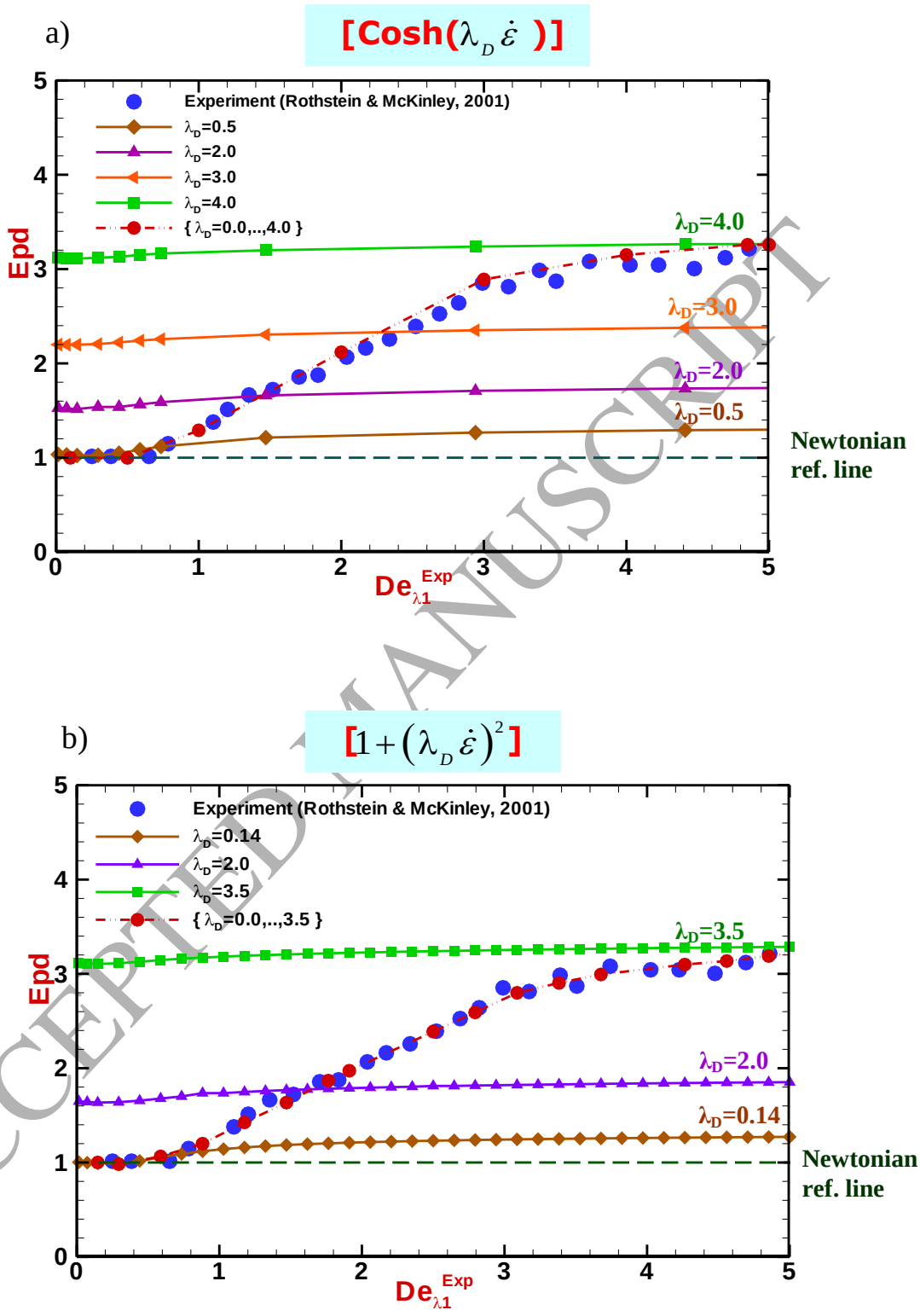

Figure 8. Normalised pressure-drop (*epd*) vs $De_{\lambda 1}^{Exp}$ for swanINNFM, a) $\cosh(\lambda_D \dot{\varepsilon})$, b)$1+(\lambda_D \dot{\varepsilon})^2$ models, λ_1-increase

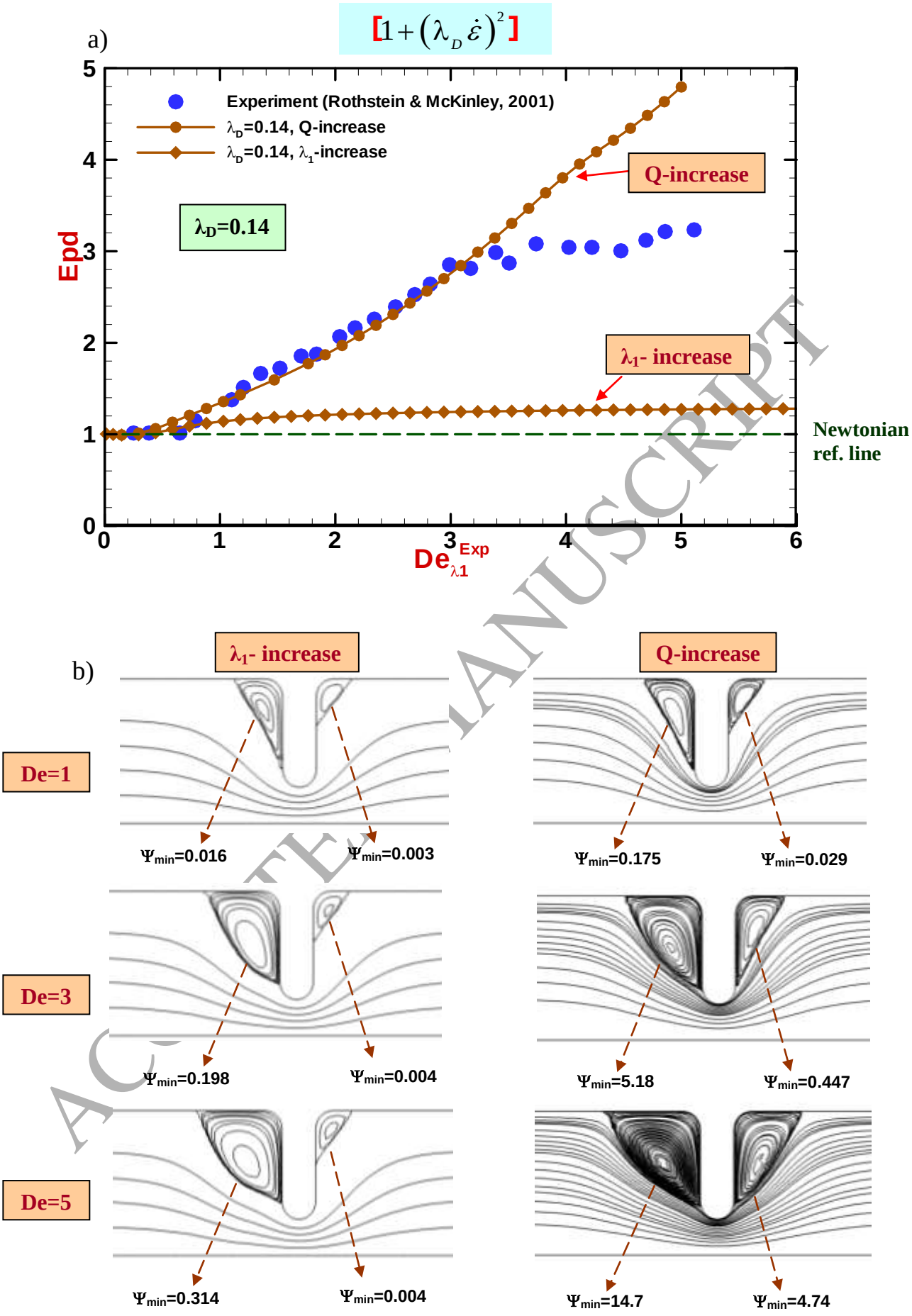

Figure 9. a) Normalised pressure-drop (*epd*) vs $De_{\lambda 1}^{Exp}$, b) stream function, λ_1-increase vs *Q*-increase, swanINNFM(q) model, λ_D=0.14, Ψ_{min}= -Ψ^*_{min}*10^{-1}

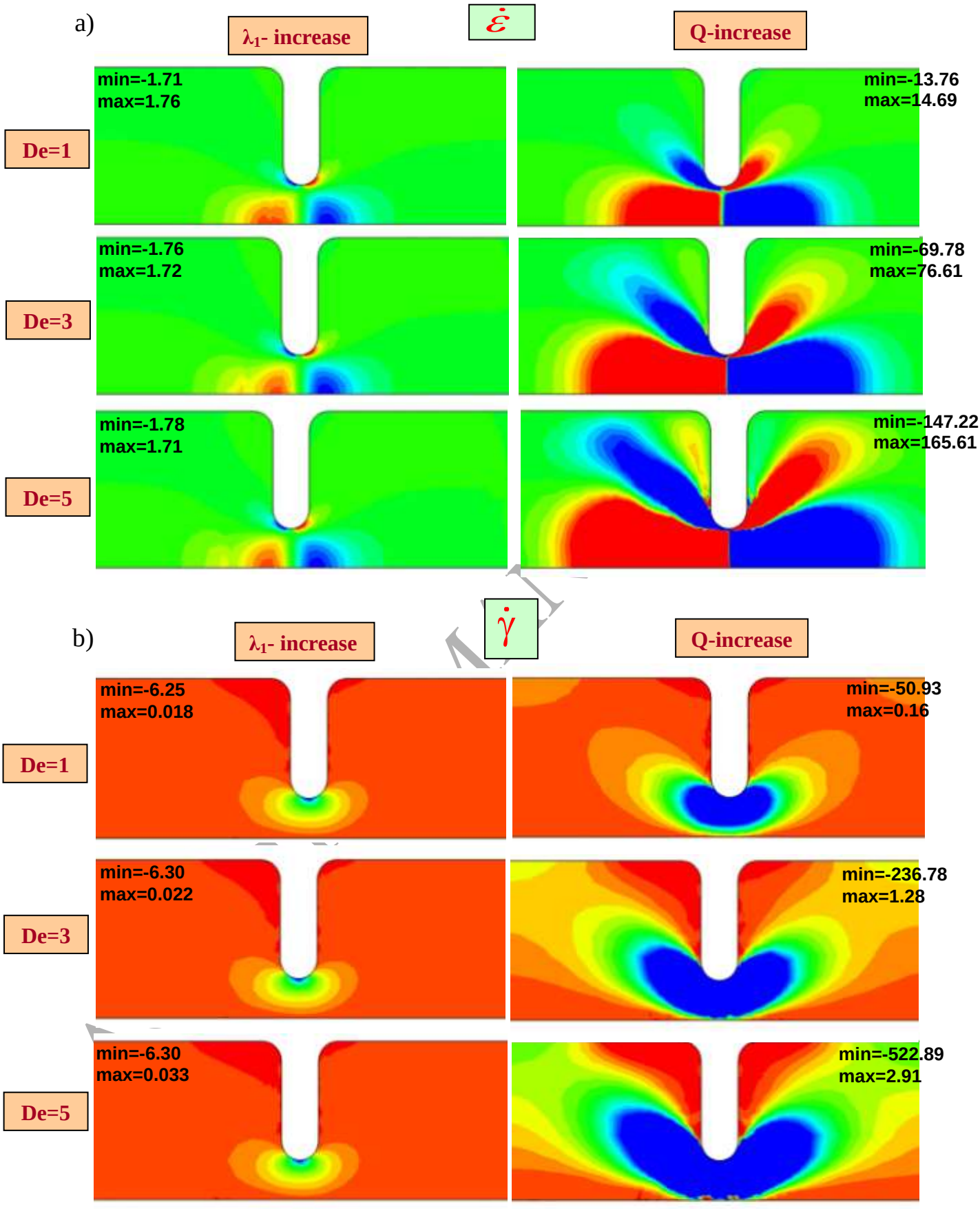
a)
$\dot{\varepsilon}$
λ1- increase
Q-increase
De=1
min=-1.71
max=1.76
min=-13.76
max=14.69
De=3
min=-1.76
max=1.72
min=-69.78
max=76.61
De=5
min=-1.78
max=1.71
min=-147.22
max=165.61
b)
$\dot{\gamma}$
λ1- increase
Q-increase
De=1
min=-6.25
max=0.018
min=-50.93
max=0.16
De=3
min=-6.30
max=0.022
min=-236.78
max=1.28
De=5
min=-6.30
max=0.033
min=-522.89
max=2.91

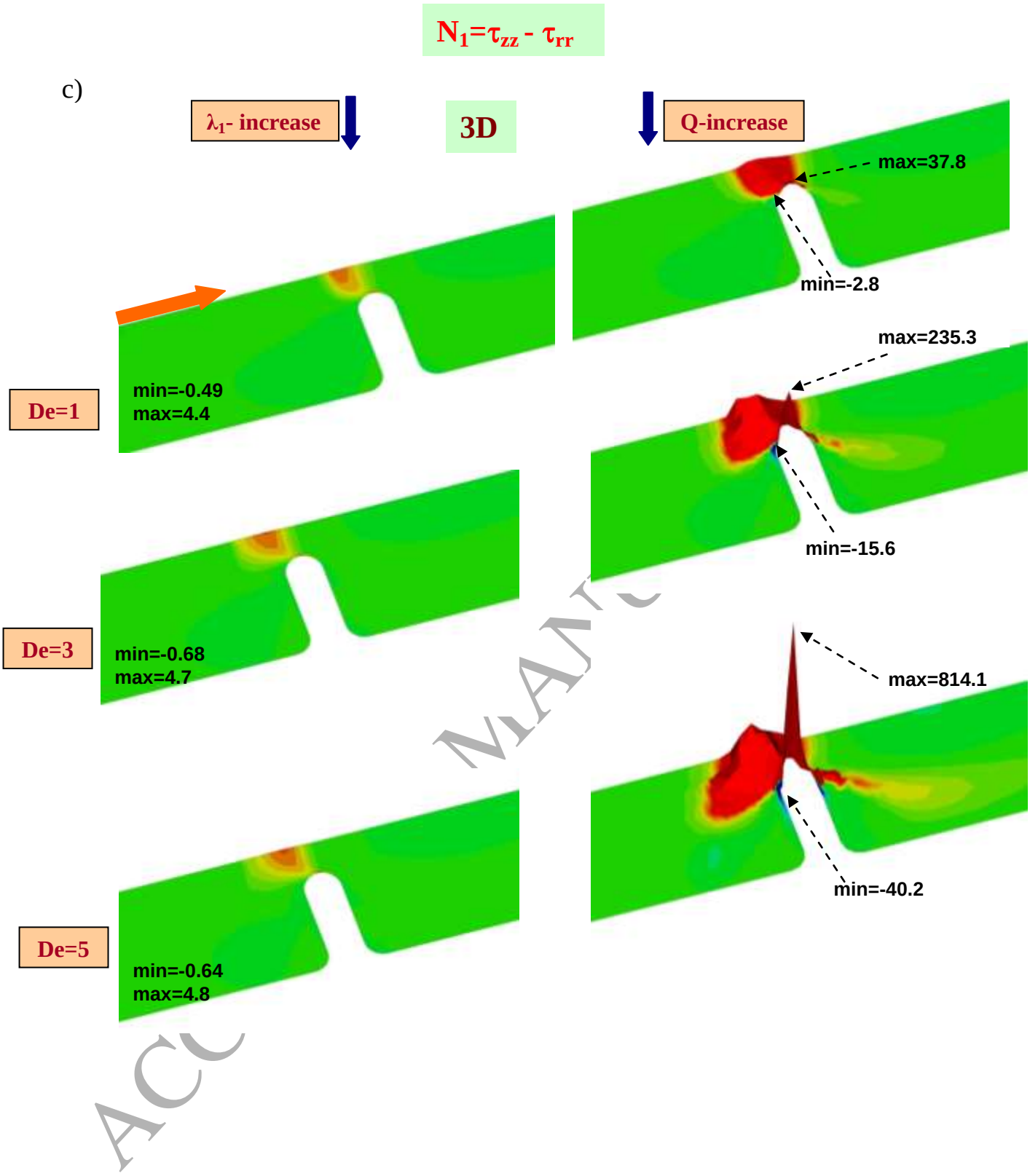
N1=τzz - τrr
c)
λ1- increase
3D
Q-increase
max=37.8
min=-2.8
De=1
min=-0.49
max=4.4
max=235.3
min=-15.6
De=3
min=-0.68
max=4.7
max=814.1
min=-40.2
De=5
min=-0.64
max=4.8

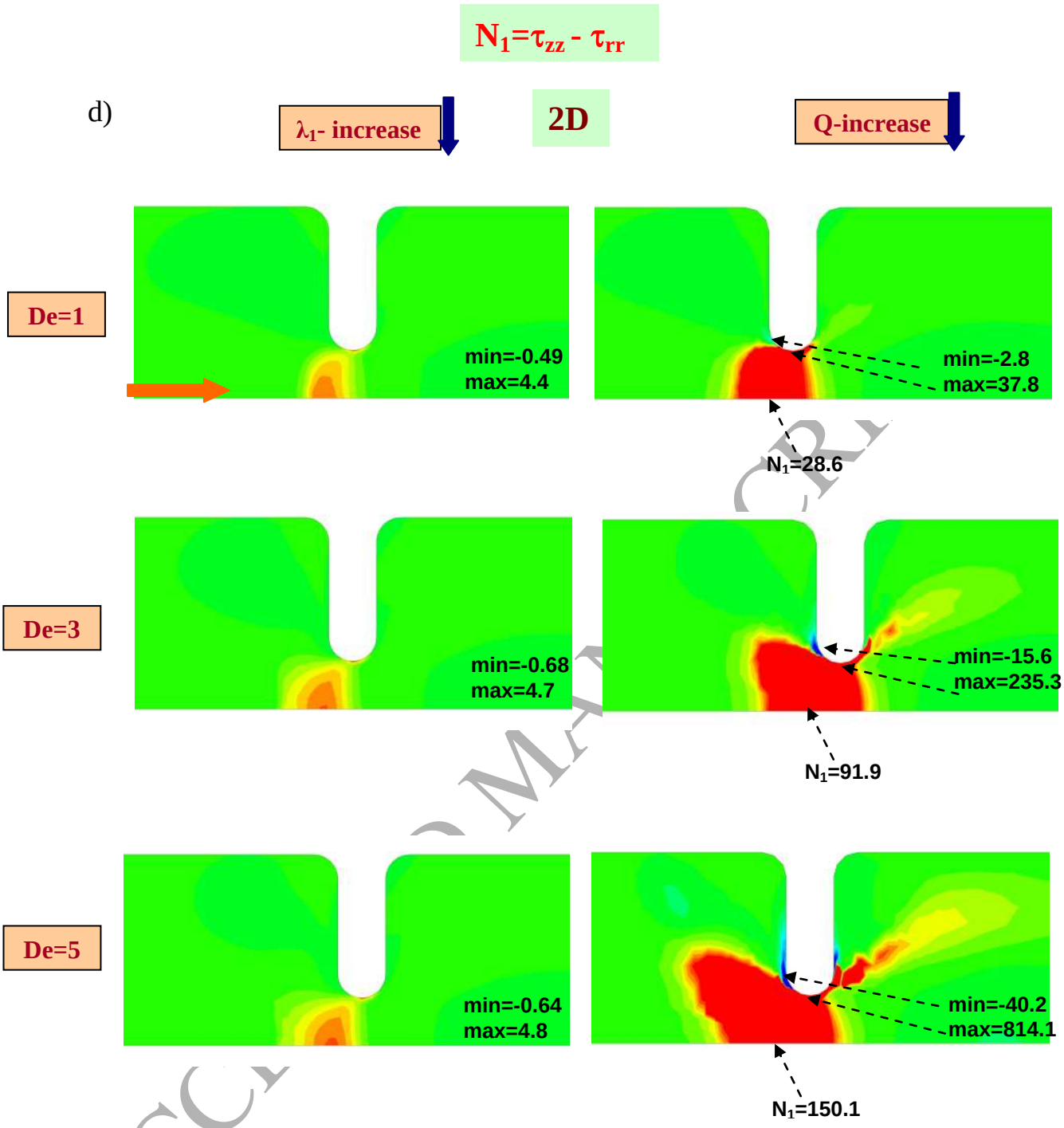

Figure 10. a) strain-rate b) shear-rate fields c, d) 3D, 2D first normal stress difference (N_1), λ_1-increase vs Q-increase, swanINNFM(q) model, λ_D=0.14

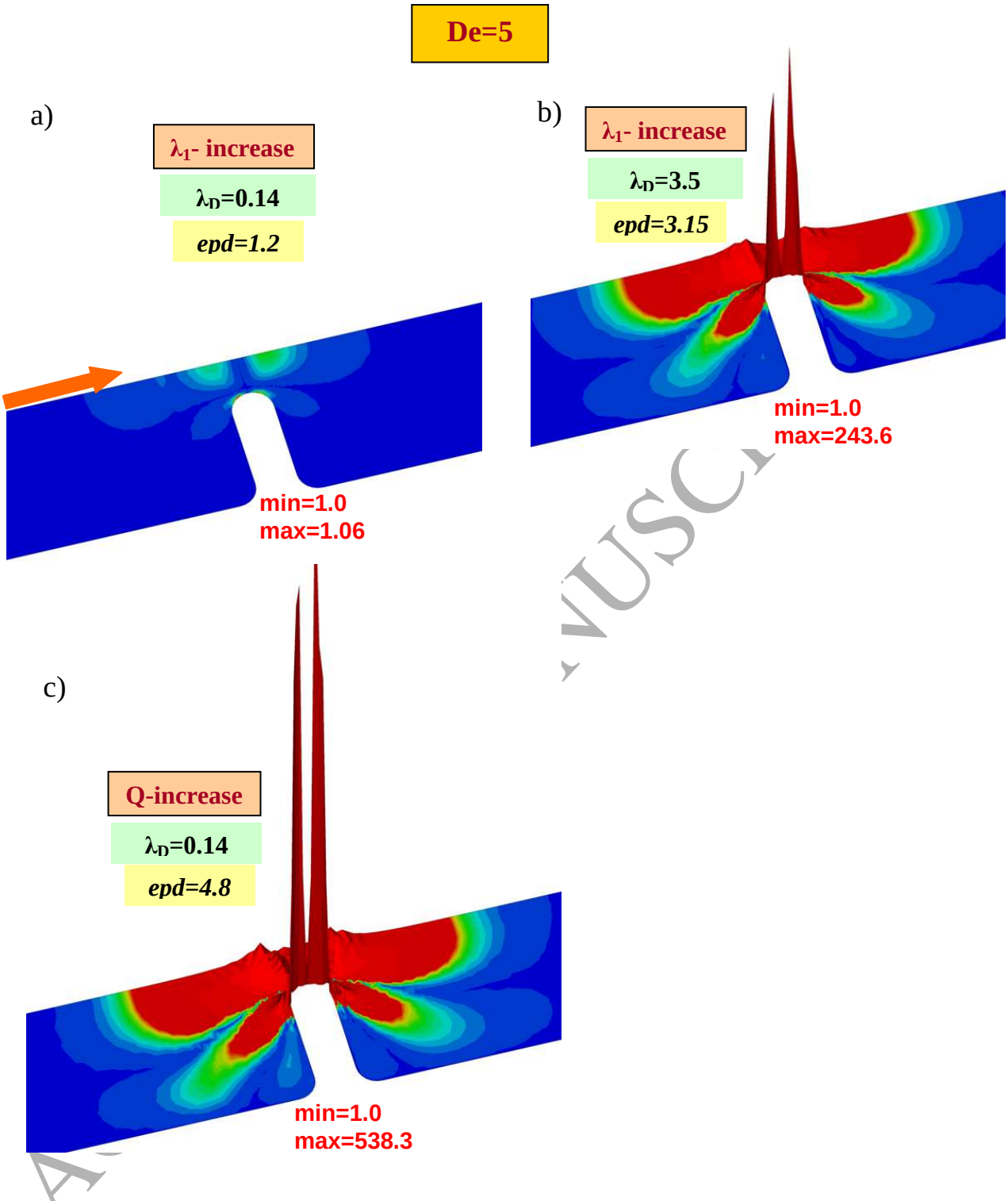

Figure 11. $\phi(\dot{\varepsilon})=1+\left(\lambda_D\dot{\varepsilon}\right)^2$, a, b) λ_1-increase (λ_D=0.14 and 3.5), c) *Q*-increase (λ_D=0.14)

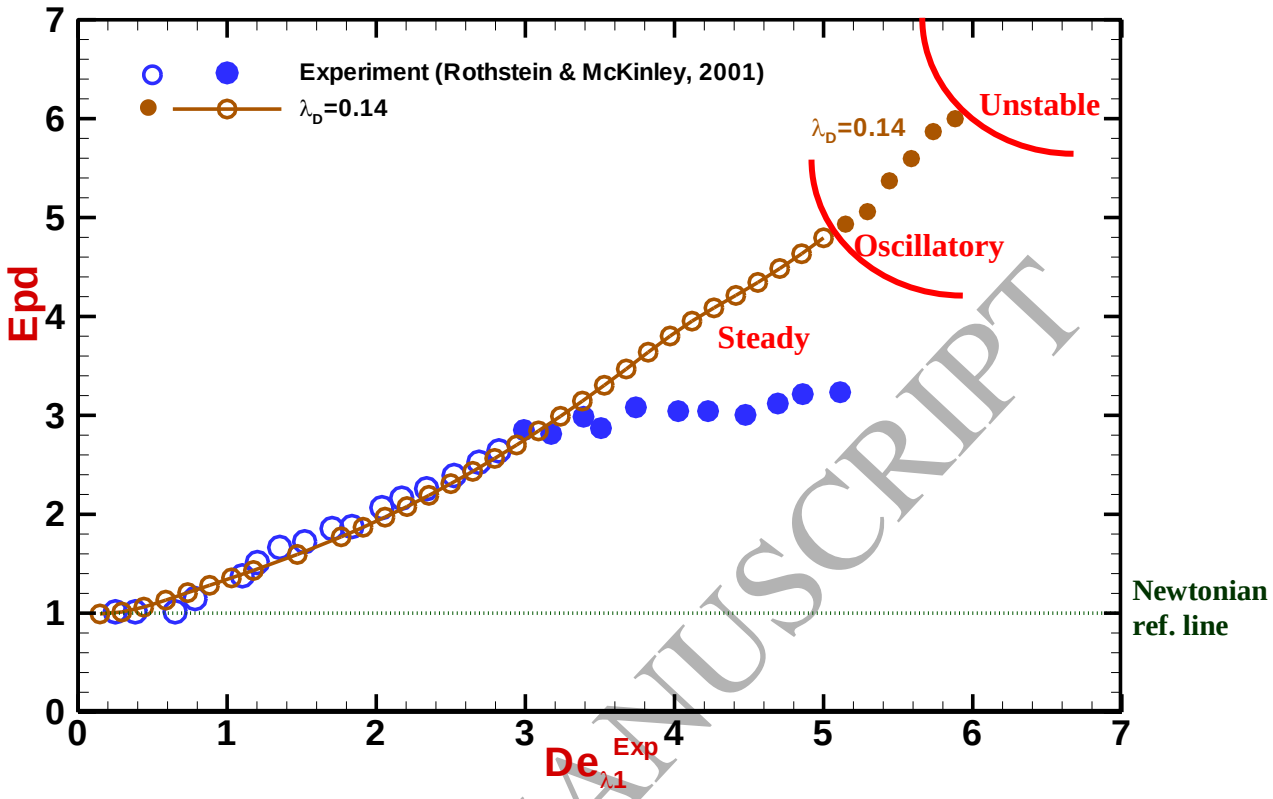

Figure 12 Normalised pressure-drop (*epd*) vs $De_{\lambda 1}^{Exp}$ for swanINNFM(q) model, flow-rate (Q) increase, λ_D=0.14, full symbols represent oscillatory flow condition

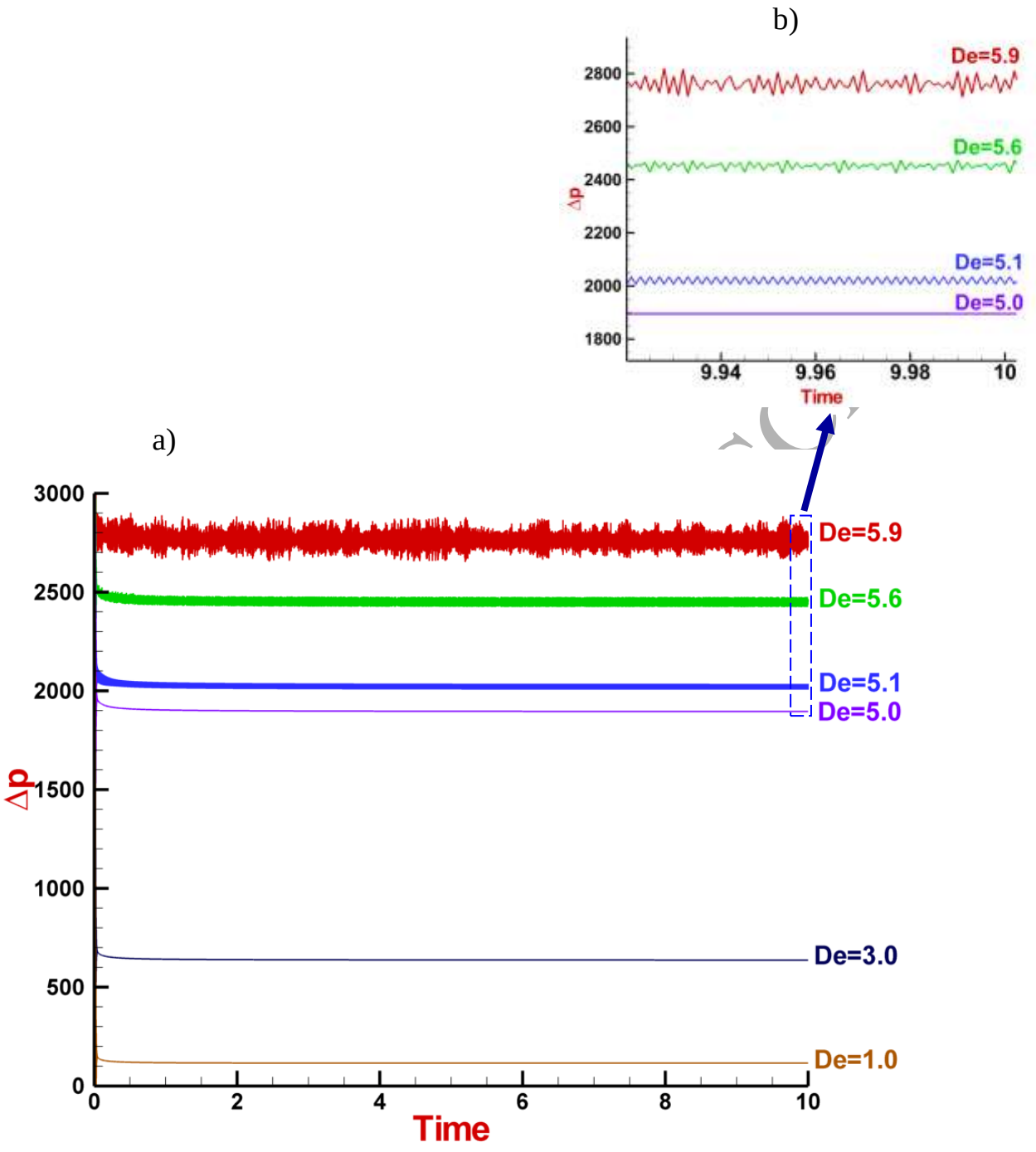

Figure 13. Temporal pressure-drop across contraction, λ_D=0.14: rising-*De*, swanINNFM(q)], *Q*-increase; a) full view, b) zoomed view

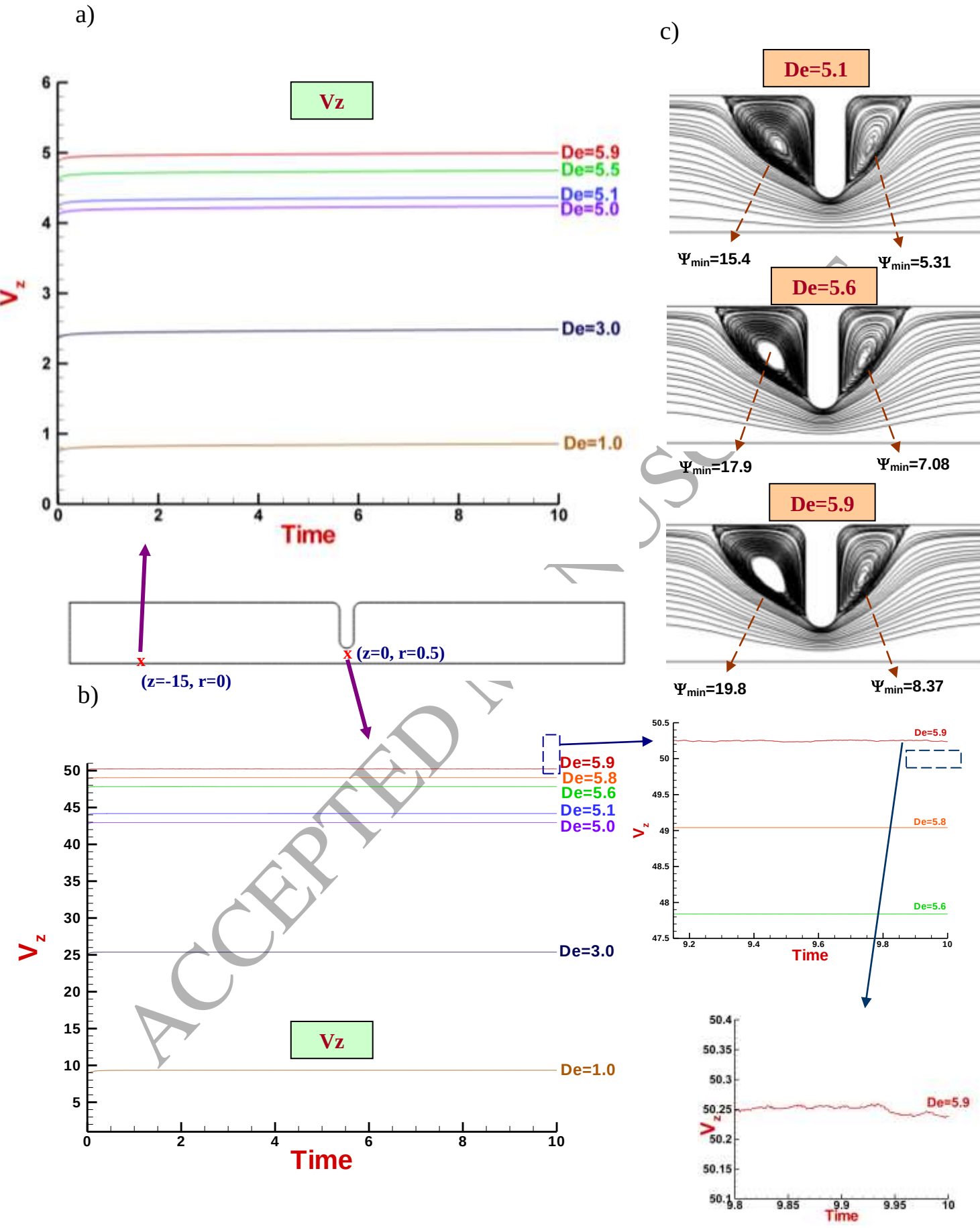

Figure 14. Temporal velocity development, λ_D=0.14: a) inlet centreline b) contraction zone; c) stream function (Ψ_{min}= -Ψ^*_{min}*10^{-1}); rising-*De*, swanINNFM(q), *Q*-increase

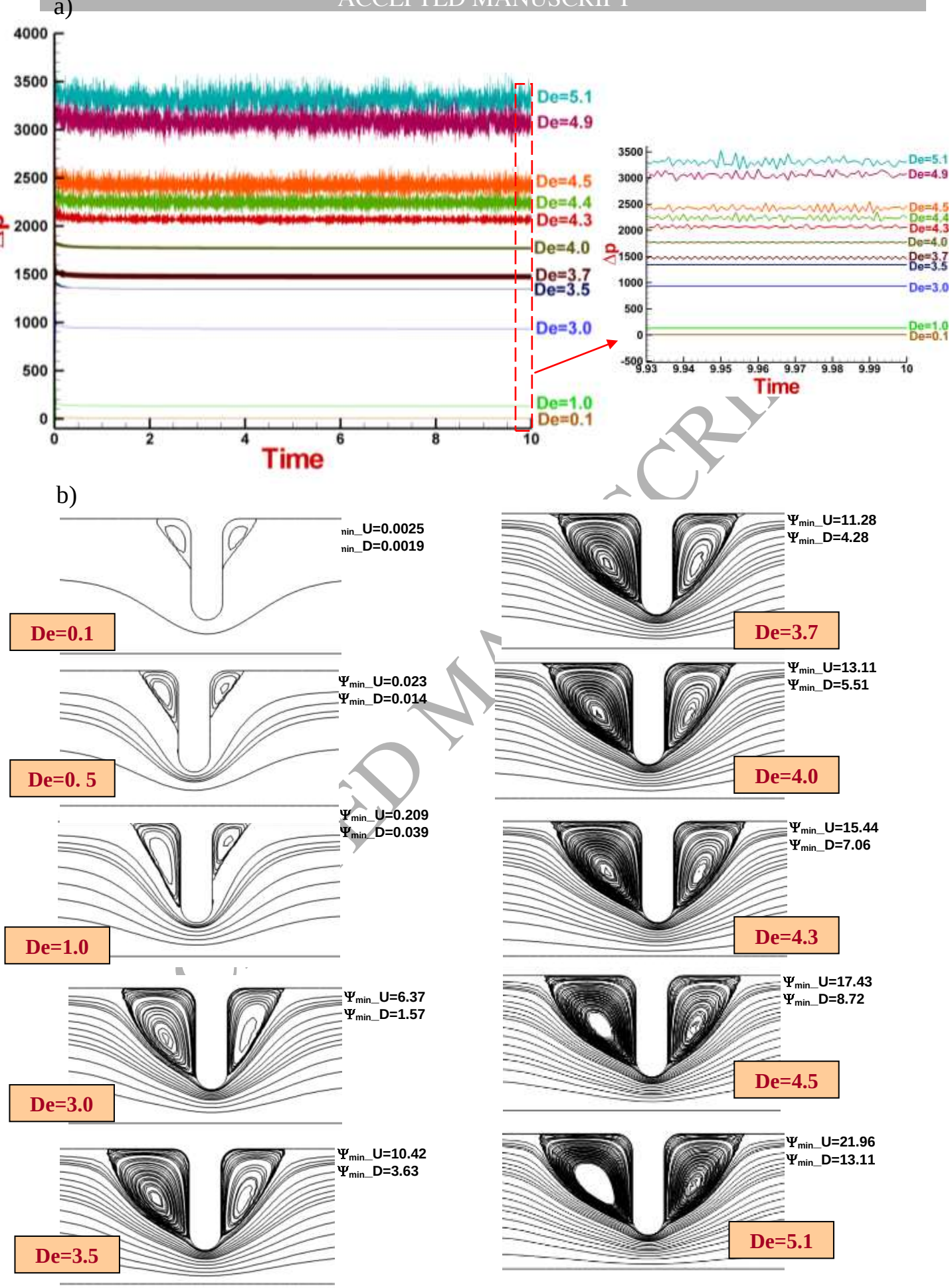

Figure 15. a) a) Temporal pressure-drop across contraction, b) stream function (Ψ_{min}= -Ψ^*_{min}*10^{-1}); rising-*De*, swanINNFM(q), λ_D=0.2, *Q*-increase

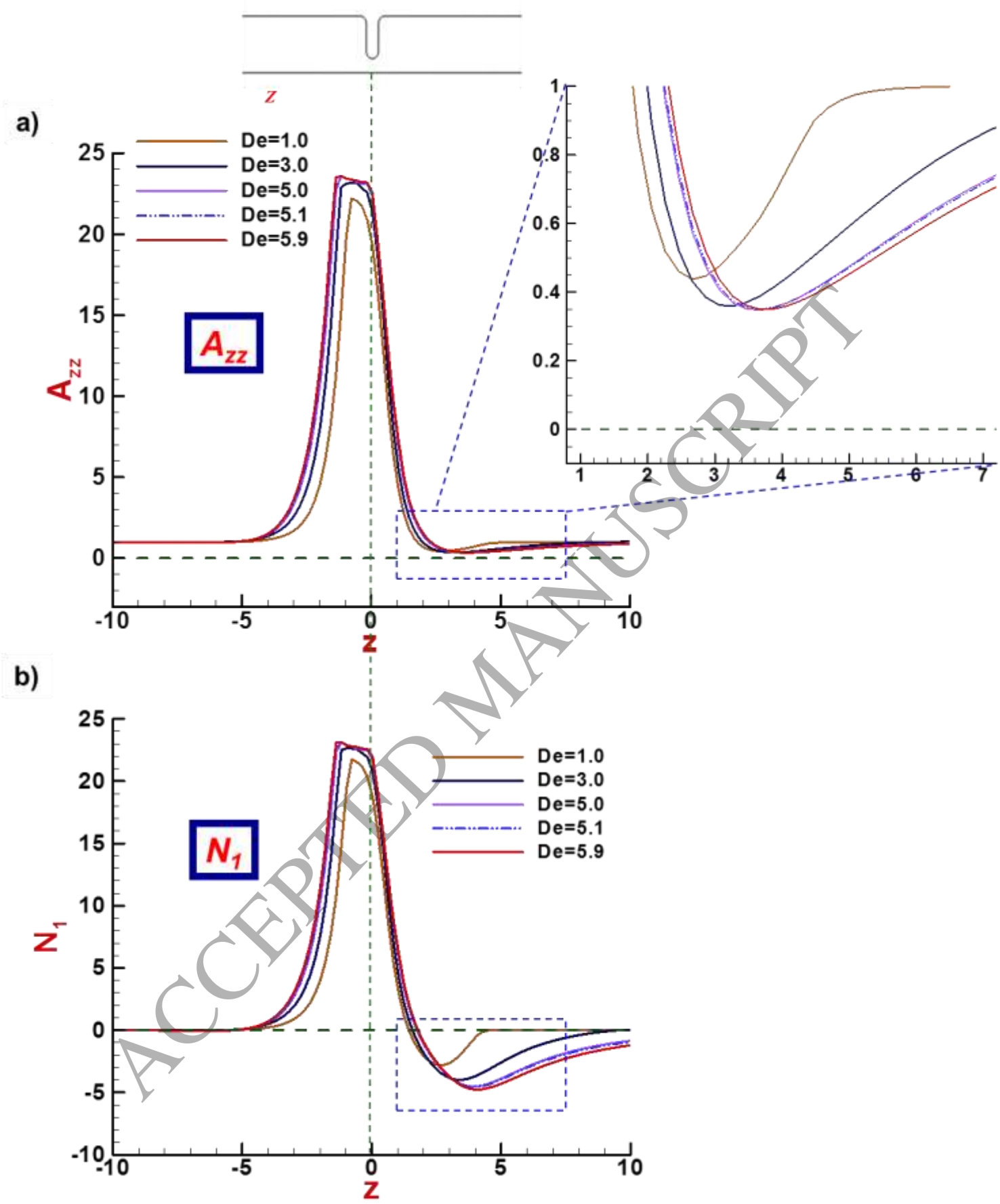

Figure 16. a) A_{zz} & b) N_1 *@ centreline* against rising-*De*, λ_D=0.14; swanINNFM(q), *Q*-increase

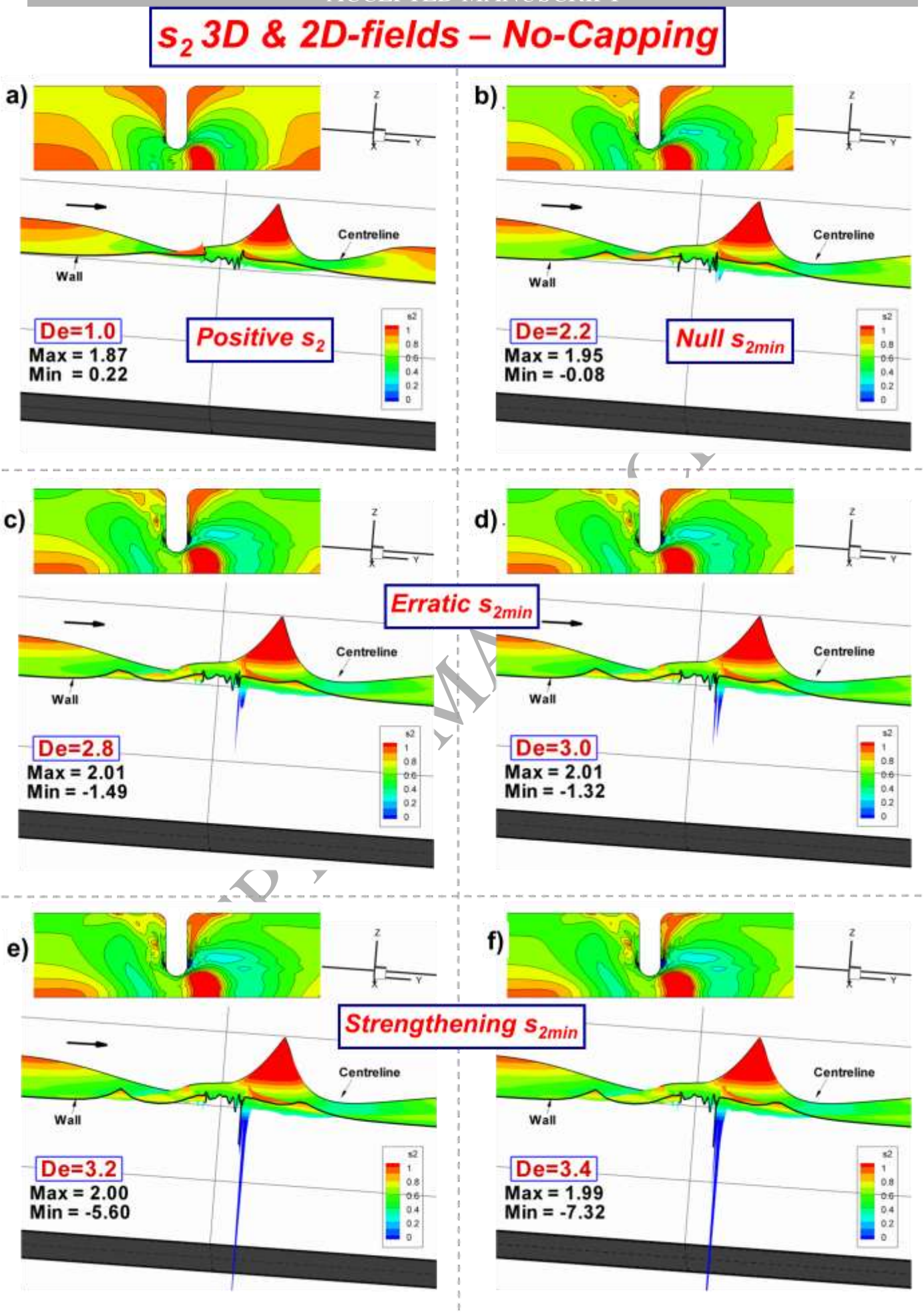

Figure 17. s_2-tracking, λ_D=0.14; No-capping strategy against rising-*De* (1.0≤*De*≤3.4); swanINNFM(q), *Q*-increase

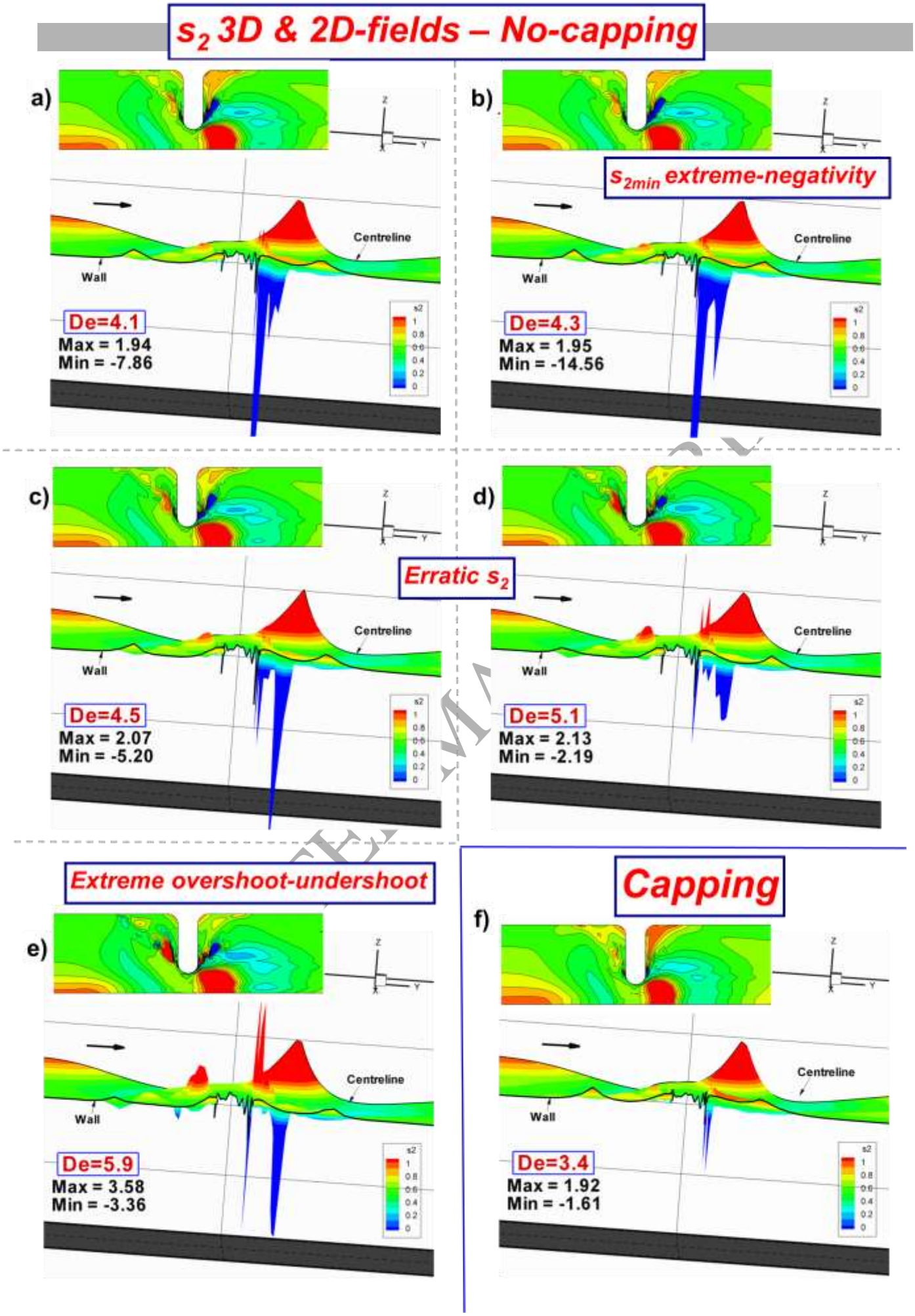

Figure 18. s_2-tracking, λ_D=0.14; a)-e): No-capping strategy against rising-*De* (4.1≤*De*≤5.9); f) Capping-strategy @ *De*=3.4; swanINNFM(q), *Q*-increase